RSC Advances

PAPER

View Article Online
View Journal | View Issue

Cite this: *RSC Adv.*, 2025, **15**, 10085

A first-principles study of dynamically stable non-toxic photovoltaic Mg_3PX_3 (X = Cl and Br) compounds

Md. Bayjid Hossain Parosh, Md Saiduzzaman, * Jahirul Islam, Nusrat Jahan Nisha* and Istiak Ahmed Ovi

Inorganic, non-toxic halide perovskites have emerged as photovoltaic field breakthroughs because of their outstanding physical properties, which make them viable for sustainable energy systems. The structural properties along with electronic, mechanical and thermal properties of Mg_3PX_3 (X = Cl, and Br) are evaluated by first-principles density functional theory (DFT) calculations executed *via* the CASTEP code employing GGA-PBE functional. The phonon dispersion results indicate that these compounds are dynamically stable because positive frequency readings show they would be suitable for experimental production. Structural and bandgap calculations required the dual use of hybrid HSE06 and GGA-PBE functionals to achieve better accuracy and resulted in 5.260 Å for Mg_3PCl_3 and 5.478 Å for Mg_3PBr_3. The calculated bandgap values are 2.297 eV for GGA-PBE and 3.093 eV for HSE06 with Mg_3PCl_3 and 1.506 eV for GGA-PBE and 2.187 eV for HSE06 with Mg_3PBr_3. The positive elastic constant C_{44} indicates structural stability in addition to unfavorable Cauchy pressure values that create brittle and rigid structural behaviors together with the Paugh's ratio and Poisson's ratio at low levels. The magnetic properties of Mg_3PX_3 (X = Cl and Br) compounds create opportunities in quantum research because these compounds exhibit diamagnetic behavior. High thermal efficiency calculated by thermal analysis enables the materials to expand their functional capabilities. Experimentation demonstrates that Mg_3PX_3 (X = Cl and Br) compounds show their exceptional optical characteristics and potential for superior photodetectors and UV protective materials. This research delivers essential knowledge about Mg_3PX_3 (X = Cl and Br), which prepares the way for the upcoming experimental development of sustainable materials for energy technologies.

Received 18th February 2025
Accepted 24th March 2025

DOI: 10.1039/d5ra01185j

rsc.li/rsc-advances

1. Introduction

In contemporary society globally individuals are faced with the ever-increasing demand for energy due to factors such as industrialization and population growth.[1] Meeting this demand is critical to the future, given that it is focused on energy storage and conversion as well as renewable energy technologies.[2] Of these, renewable energy sources such as solar cells have a special importance in minimizing the dependency on known depleting resources like fossil fuels.[3] Additionally, sourcing energy from natural resources has greatly aided the reduction of greenhouse gas emissions, the use of oil, and the degradation of the environment universally.[4]

Photovoltaic cells have become vital aspects of green energy technologies because they can effectively generate electrical energy from solar power.[5] Over the past few years, various perovskite-based materials have attracted massive interest in solar energy systems because of their exceptional photovoltaic and energy conversion characteristics.[6] First investigated nearly two decades ago as piezoelectric and ferroelectric compounds in metal oxides, perovskites have transformed into versatile material for thin films of absorber layer and other solar cell related.[7] The exceptional flexibility and performance of certain materials have established them as essential components in LEDs and renewable energy technologies, driving global research and development to satisfy the rising demand for sustainable energy solutions.[8] Many materials are inherently limited, yet practical application of many materials requires materials that combine physical stability and high quality, but often the materials required for high-performance devices do not give both qualities.[9] So, they are actively working to develop cost-effective alternatives that can stand up to extreme conditions without degrading.[10] The perovskite-based compounds stand out as particularly attractive in that they exhibit properties that make them attractive for use in sensors, photovoltaics, optoelectronics, high-temperature superconductors, and semiconductors.[11] Specific to need advanced nanostructures, such as nanowires, nanocrystals, and nanoparticles can be created, with unique structural adaptability.[12] The versatility of perovskite-based systems implies that they will provide a more

Department of Materials Science and Engineering, Khulna University of Engineering & Technology (KUET), Khulna-9203, Bangladesh. E-mail: msaiduzzaman@mse.kuet.ac.bd; nusrat.jahan.nisha.mse@gmail.com

economical and flexible route to advanced technologies than conventional silicon-based ones.[13]

A_3MX_3 compounds (A = Mg, Ca, Sr, Ba; M = N, P, As, Sb; X = F, Cl, Br, I) utilized in photovoltaic devices were the subject of recent research. Band-edge transitions, tunneling, thermal characterization, bandgap, and estimated efficacy are among the properties that these materials may exhibit.[14] The analysis showed that these compounds possess properties similar to halide perovskites currently used in solar cell technology. Ghosh *et al.* (2024) investigated the physical characteristics of inorganic halide A_3BX_3 perovskites used as the absorber layer for solar cells with better effectiveness. The study also depicts that Sr_3AsI_3 solar cells retain more than 28% of power conversion efficiency (PCE) in terms of conversion of energy.[15] Hossain *et al.*, (2024) utilized first-principles DFT calculations to investigate the structural, electronic, mechanical, optical, thermodynamic, and thermoelectric properties of lead-free Sr_3ZBr_3 (Z = As, Sb) compounds with their direct band gap semiconducting nature, improved optical and mechanical properties under pressure, and high thermoelectric performance, and are tantamount for optoelectronic and thermoelectric applications.[16] Based on the results of first principles DFT calculation, the pressure-induced reduction of the bandgap and enhanced optical and mechanical properties along with high thermoelectric performance, Abdulhussein H. A., *et al.*, (2025) suggest that lead-free cubic Ca_3SbX_3 (X = Cl, Br) is a potential candidate for use as the solar absorber, surgical instrument, and thermoelectric devices.[17] In the study, Chahar *et al.* (2024) used GGA and HSE06 functionals to compute the structural, electronic, and optical properties of the novel perovskite halide Mg_3AsCl_3 with an indirect bandgap, low reflectivity, and outstanding dielectric properties which make it a promising candidate for various electronic device applications.[18] Apurba *et al.* [2024] investigated the Ca_3PX_3 (X = I, Br, Cl) system physical properties and calculated the tunability of their band gaps under tensile and compressive strain.[19] This study utilizes DFT calculations to investigate the structural, mechanical, electronic, and optical properties of Mg_3PF_3 fluoro-perovskite, demonstrating its ductility, a direct bandgap of 3.88 eV, and significant potential for solar cell applications owing to its advantageous dielectric properties and ionic bonding characteristics.[20] The ability of thermoelectric materials to transform thermal energy into electrical energy makes them essential for use in cooling systems, power generation, and sensor technologies, among other uses.

In this study, DFT calculations are performed employing first principles to study the properties of the new Mg_3PX_3 (X = Cl, Br) compounds in the vacuum case and the hydrostatic pressure case. Overall, one aims to understand the physical properties of these lead-free, non-toxic materials with the application of hydrostatic pressure and to investigate the structural and electronic transitions under such pressure. The band gap tunability under hydrostatic pressure is systematically considered using various exchange–correlation functionals such as GGA-WC, Hybrid-HSE06, GGA-PBESol, and GGA-PBE to verify their accuracy in predicting band gap values. To our knowledge, there have been no previous theoretical or experimental studies on these compounds. This research is intended to generate insights that may be of value in the development of optoelectronic as well as photovoltaic technologies.

2. Computational details

This entire calculation is based on DFT (First principal approach) calculation with CASTEP (Cambridge Serial Total Energy Package), which explains the different properties of materials. To find new properties, it's very helpful to use. This program demystifies the calculations of material scientists. Perdew–Burke–Ernzerhof's (PBE) function with the Generalized Gradient Approximation (GGA) function is used in this particular work.[21] Vanderbilt-type ultra-soft pseudopotentials are used to get a more accurate picture of how electrons interact.[22] The energy cut-off is 700 eV used with Monkhorst–Pack mode for achieving better accuracy in the study. 8 × 8 × 8 *k*-point grids are deployed to reveal the Brillouin zone well. The cell optimization was taken "full" to get results.[23] Energy tolerance is 5.0×10^{-6} eV per atom, a maximum force threshold of 0.01 eV $Å^{-1}$, and a maximum atomic movement of 5.0×10^{-4} Å. The Broyden–Fletcher–Goldfarb–Shanno (BFGS) algorithm of CASTEP is used to get much more accurate results. It has strict convergence standards that cover the highest stress and movement, as well as energy tolerance factors.[24] The convergence tolerance quality was ultra-fine. The convergence energy was taken 5×10^{-6} eV per atom for the calculation. A maximum of 100 iterations were taken with the BFGS algorithm. The pseudopotential OTFG ultrasoft was taken to ensure accuracy. SCF tolerance 5×10^{-7} with 100 SCF cycles and the convergence window was selected 3 for better accuracy. The maximum for convergence tolerance stress was 0.02 GPa taken. FFT grid density was taken as "Precise," and the augmentation density scaling factor was 1.5.[25] Spin polarization was selected as non-polarized. In magnetic calculation, the "Spin polarization" was selected as "co-linear".[26]

3. Result and discussion

3.1 Structural properties

In the context of DFT, structural property mainly denotes the properties that refer to the physical characteristics of a compound that describe the structure of the compound.[27] To determine new material as well as new properties of a material, structural property is a must because without crystal stability, it's not feasible to study the compound. A stable crystal structure is a prerequisite for determining other properties. The optimized structure of the studied compound Mg_3PBr_3 is shown in Fig. 1, illustrated with VESTA. Where atoms are arranged in the exact ideal position of a photovoltaic compound. Mg is placed in the 3d Wyckoff position (0.5, 0, 0), P is placed in the center with the Wyckoff position 1a (0, 0, 0), and lastly, X which denotes the halogens are located in 3c Wyckoff position with the coordinate of (0, 0.5, 0.5).[28] As the atoms are located, it's essential to ensure they are stable in those positions. The factors helping to understand the crystal stability of the compound are the tolerance factor (*t*) and formation enthalpy.

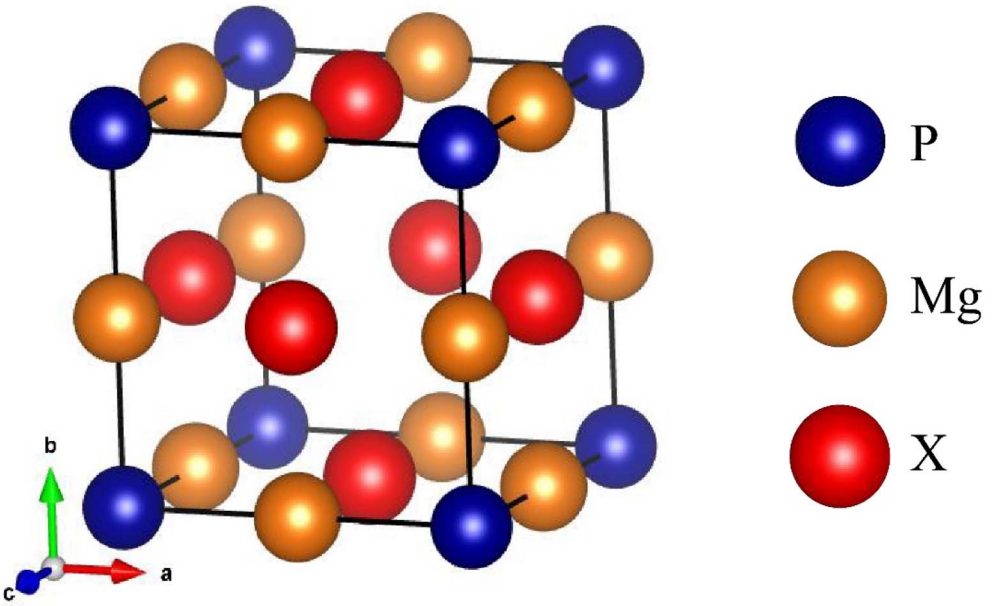

Fig. 1 Crystal structure of Mg_3PX_3 (X = Cl and Br).

Since this investigated compound in this study hasn't been studied or synthesized yet so additional data on Formation enthalpy and tolerance factor may ensure the crystal's stability. Formation enthalpy confirms the thermodynamic stability of the compound, while the tolerance factor ensures the cubic stability for the novel photovoltaic Mg_3PX_3 (X = Cl and Br) compound.

$$t = \frac{R_{Mg} + R_x}{\sqrt{2}(R_P + R_x)} \quad (1)$$

$$E_f = \frac{E_{tot}(Mg_3PX_3) - 3E_s(Mg) - E_s(P) - 3E_s(X)}{N} \quad (2)$$

Here, in eqn (1), R_{Mg} refers to the ionic radius of the Mg atom, RP represents the ionic radius of the P atom, and R_x represents the ionic radius of the halogen group. Halogen (Cl and Br) is varied in this study.

In eqn (2), E_s denotes the enthalpy of the specific compound. E_{tot} denotes the total computed energy for the whole compound. N is the total number of atoms present in the structure. The structural data are plotted in Table 1, such as the lattice parameter a (Å), cell volume V (Å^3), and formation enthalpy ΔE_f (eV per atom).

The condition for being thermodynamically stable, the formation enthalpy, must remain negative of the compound.[30] Table 1 shows the data of the optimized structure, and there is a negative value of formation enthalpy in each case, which validates that the studied photovoltaic compound is thermodynamically stable with a negative value. The bromine-based compound has higher negative formation energy magnitudes than Mg_3PCl_3. Apart from the thermodynamic stability, there is also cubic stability. A compound should be considered a cubically stable structure when the tolerance factor of a compound should remain 0.813 to 1.107.[31] From Table 1, this studied geometrically optimized structure has a fine tolerance factor where the condition is fully carried out. Following the data plotted in Table 1 confirms the crystal stability of the compound. This optimized structure complies with all the conditions of stability. Table 1 also represents the basic structural data of the compound, such as cell volume and lattice parameters. The cell volume for Mg_3PCl_3 and Mg_3PBr_3 is 145.586 Å^3 and 164.397 Å^3, respectively. The lattice parameters are 5.260 Å and 5.478 Å, similar to the previous data presented in Table 1. This indicates the accuracy of this work. Where all the data is carried by substituting the halogen site of the compound with Cl and Br, a trend is primarily observed when a bigger halogen is substituted to the site of the compound by replacing both cell volume and lattice parameter of the compound is increasing. As the atomic radius of the halogen increases, the total cell volume and lattice parameter increase.

Table 1 Lattice constant a (Å), cell volume V (Å^3), formation enthalpy ΔE_f (eV per atom) and tolerance factor t for Mg_3PX_3 (X = Cl and Br) with different functional and previous work

	Lattice constant, a (Å)			Cell volume, V (Å^3)			
Compound	GGA-PBE	Previous work [GGA-PBE][29]	Hybrid HSE06	GGA-PBE	Hybrid HSE06	Enthalpy, ΔE_f (eV per atom)	Tolerance factor, t
Mg_3PCl_3	5.26	5.24	5.22	145.59	142.16	−3.60	0.82
Mg_3PBr_3	5.48	5.46	5.43	164.40	159.83	−3.32	0.81

Table 2 Bond length for Mg_3PX_3 (X = Cl and Br)

Compound	Bond	Length (Å)
Mg_3PCl_3	P–Cl	3.72
	Mg–Cl	2.63
	Mg–P	2.63
Mg_3PBr_3	P–Br	3.87
	Mg–Br	2.74
	Mg–P	2.74

It also can be said that in Mg_3PCl_3, the atoms of this compound are more closely packed as their atomic radius and cell volume are lower compared to Mg_3PBr_3.

Table 2 shows the bond length data of the studied material. Generally, the distance between two nuclei of a bond in an atom is termed this distance. Here, the bonding between Mg–Cl and Mg–P is the shortest, which denotes they have a strongly bonded structure than other bonding. When a heavier halogen is placed in the X position, the bond length increases in the structure. One thing to notice is that Mg is bonding similarly strongly with P and X atoms here. The shorter the bond length, the stronger the bond is. Among them, P–X shows the lowest bonding strength, which indicates that the nuclei of P and X are much closer than other bonded nuclei.

3.1.1 Phonon dispersion. Phonon dispersion represents the dependence of phonon frequencies on their wave vectors and the position in the Brillouin zone that reveals information concerning the stacking periodic system and heat characteristics of a given material. Mg_3PCl_3 is another compound with a positive phonon dynamical matrix at high symmetry points *X*, *R*, *M*, *Γ*, and *X*, as shown in the following Fig. 2 for phonon frequency (THz).[32,33] The acoustic branches starting from the *Γ* point at $\omega = 0$ are related to low-frequency lattice phonons, which are important for heat conductance. The optic branches observed at high frequencies are related to atomic oscillations out of phase due to strong interatomic forces.[34] Small numbers of transitions with continuous change in acoustic modes and separate optical branches suggest effective acoustic phonon transport and low phonon scattering, as well as strong bonding.[35] The highest frequency modes (~10 THz) underpin light atomic masses and strong bonding in Mg_3PCl_3, which suggests that this material is thermally stable and could also be used for high-performance applications where good thermal conductivity is desirable. The overall frequencies compared with Mg_3PCl_3 are a bit lower and with a maximal of about 9 THz, which might reflect the presence of heavier Br atoms lowering the vibrational frequencies. Like the acoustic branches necessary for thermal conductivity, the optical ones also increase at a similar gradient, though crowding more closely indicates weaker interatomic forces here compared to Mg_3PCl_3. That is, there could be reduced phonon scattering with the atoms being closer, leading to reduced thermal conductivity.[36] The comparative study shows that although Mg_3PBr_3 remains stable, the vibrational behavior indicates a comparatively lower phonon transport efficiency, mainly due to the increased atomic mass and lower maximum phonon frequencies.[37]

3.2 Electronic properties

The band structure is a vital descriptive tool for showing how electronic energy levels are distributed based on crystal momentum within the Brillouin zone of materials.[38] Knowledge of band structure gives scientists vital information about material conductivity and optical features as well as their suitability in photovoltaics and optoelectronics applications.[39] The band structure shows energy (*E*) values along the vertical axis, where high-symmetry points in the Brillouin zone appear on the horizontal axis. Crystal lattice directions (*Γ*, *X*, *R*, *M*) function as high-symmetry points for evaluating electronic states in the crystal structure.[40] The valence band (VB) holds electrons at absolute zero temperature within its top energy range, and the conduction band (CB) maintains its bottom energy range with no electrons at this temperature point. A reference point named the Fermi level (E_F) defines what states are occupied and

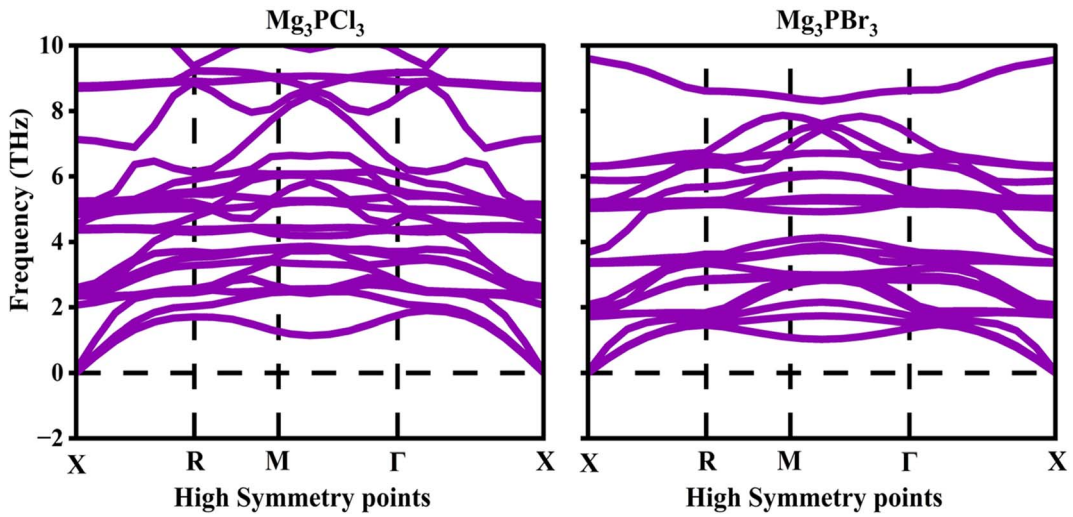

Fig. 2 Phonon spectra of Mg_3PX_3 (X = Cl and Br).

unoccupied in electronics.[41] A material functions as a metal, semiconductor, or insulator based on the maximum valence band-conduction band minimum energy gap (E_g). Semiconductor and insulating materials depend fundamentally on the band gap energy parameter because it determines optical absorption ability, electrical conduction rate, and device operational characteristics.[42]

In Fig. 3, the band structure calculations for Mg_3PCl_3 and Mg_3PBr_3 used two exchange–correlation functionals, namely GGA-PBE and HSE06, to generate the graphs. The calculated band gap by GGA-PBE functional for Mg_3PCl_3 amounts to 2.297 eV, but when HSE06 functional is used, it predicts a higher band gap value of 3.093 eV. The band gap estimation for Mg_3PBr_3 using GGA-PBE leads to 1.506 eV, but when HSE06 is applied, it results in 2.187 eV. The band structures demonstrate direct band-gap characteristics at the Γ point because VBM and CBM energies occur at the identical high-symmetry point of the Brillouin zone. The larger band gaps predicted by the HSE06 functional relative to GGA-PBE are in line with the general tendency of HSE06 to yield more accurate values for band gaps, due to the inclusion of some fraction of exact Hartree–Fock exchange, which corrects the underestimation of band gaps by GGA-PBE.[43,44] The perspective drawn from using both GGA-PBE and HSE06 functionals emphasizes the selection of an efficient exchange–correlation functional to ensure an accurate prediction of the band gap.[44] The GGA-PBE Method incorporates a band structure model that ignores the effects of electronic exchange and correlation, and this tends to underestimate the band gap value deficits for both Mg_3PCl_3, which is 2.297 eV, and Mg_3PBr_3, which is 1.506 eV. The HSE06, which accurately predicts the band gap of both Mg_3PCl_3 and Mg_3PBr_3, gives more accurate band gaps of 3.093 eV and 2.187 eV, respectively. This tendency for other reports on the halide perovskites that have demonstrated previously a band gap lower than HSE06 has been achieved for these compounds.[41]

The Fig. 4 bar chart illustrates band gaps of Mg_3PX_3 (X = Cl and Br) compounds obtained from GGA-WC, GGA-PBEsol, GGA-PBE, and Hybrid-HSE06 exchange–correlation functionals. The band gaps are stated in eV units. The band gaps starting from value 0 up to four eV are presented visually. It is noticed that the Hybrid-HSE06 method provided the greatest gaps, as expected from more complicated systems that involve the use of exact exchange. Gaps from GGA-PBE are always lower than the other methods in this comparison, showing a great value of band gap underestimation. The GGA-WC and GGA-PBEsol provide values that are more favorable than these two but do not reach the

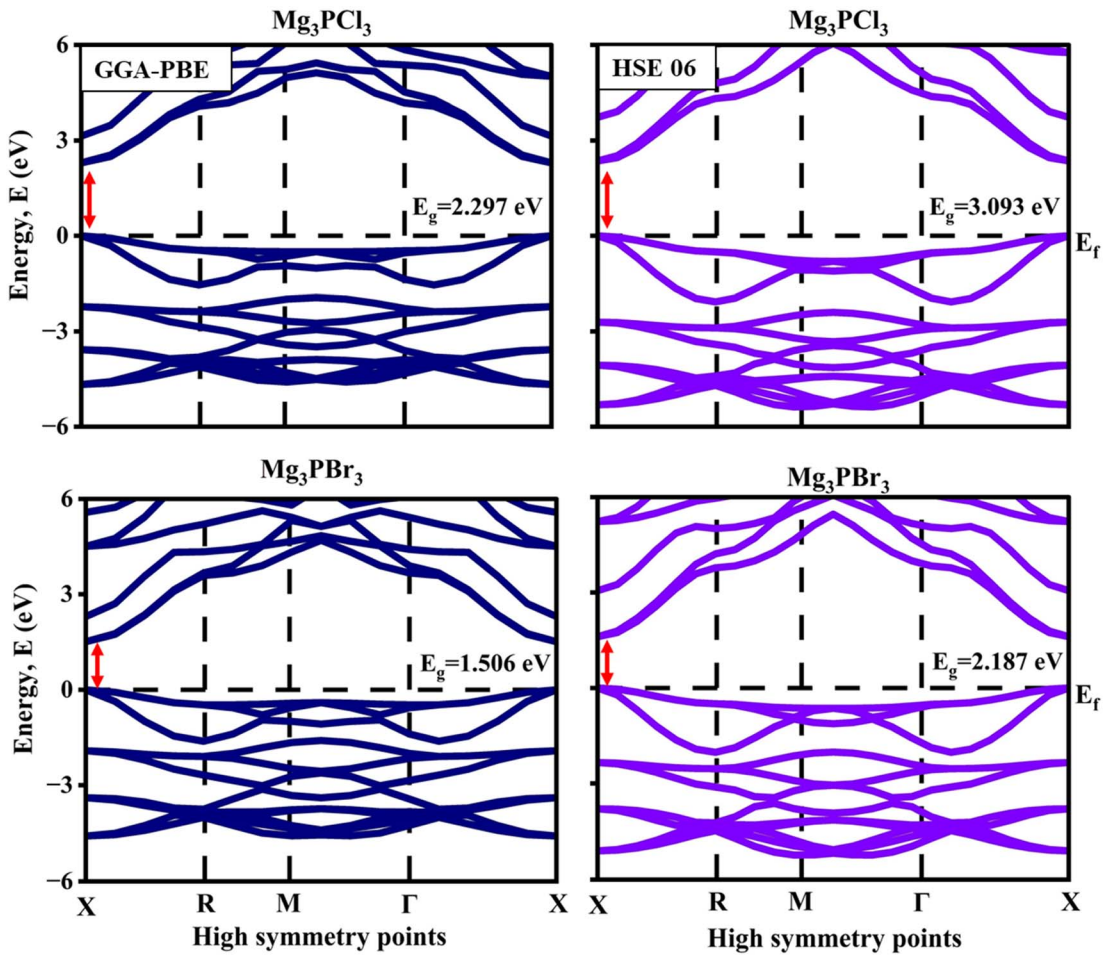

Fig. 3 Band structure of Mg_3PX_3 (X = Cl and Br) with GGA-PBE and HSE06 functional.

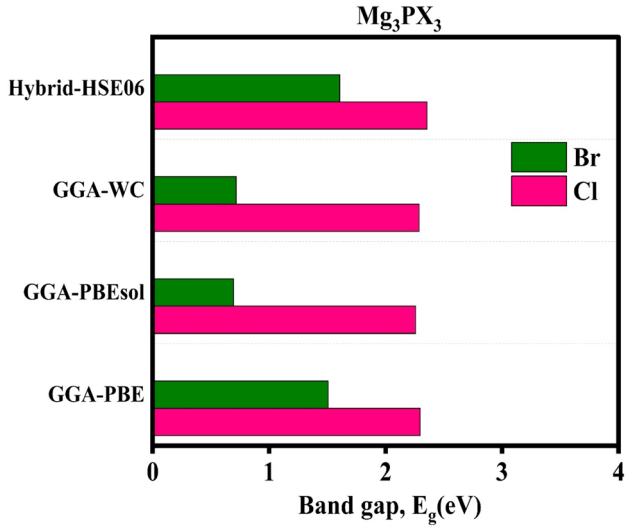

Fig. 4 Comparison of the Band structure of Mg_3PX_3 (X = Cl and Br) with varying functional.

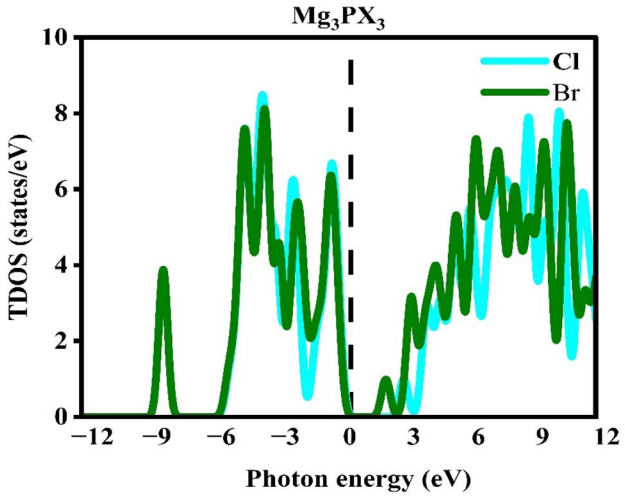

Fig. 5 Total density of states of Mg_3PX_3 (X = Cl and Br).

same results as GGA-PBE.[45] This comparison highlights the importance of functional choice in predicting electronic properties, with HSE06 being the most reliable for accurate band gap estimation in optoelectronic materials.

The band structure analysis of Mg_3PCl_3 and Mg_3PBr_3 reveals their semiconducting nature with direct band gaps, making them suitable for optoelectronic applications. The HSE06 functional provides more accurate band gap predictions compared to GGA-PBE, highlighting the importance of advanced exchange–correlation functionals in computational materials science. The larger band gap of Mg_3PCl_3 compared to Mg_3PBr_3 reflects the influence of halide electronegativity on electronic properties. These insights provide a foundation for further experimental and theoretical studies on these materials for advanced optoelectronic devices. Table 3 represents the band gap with other functional like GGA-WC and GGA-PBEsol with the comparison of previous data.

Fig. 5 reveals the Total density of states (TDOS), and Fig. 6 shows the Partial Density of States (PDOS) of Mg_3PCl_3 and Mg_3PBr_3, giving important information regarding the electronic structure and their physical properties. The DOS plots demonstrate the distribution of electronic states about energy (eV), with the *x*-axis representing energy levels and the *y*-axis indicating the number of states per unit of energy. As with both compounds, the importance of the valence band (VB) is dominant and shifted towards the lower energy range (negative values), while the conduction band (CB) occupies the highest degree of positive energy. The presence of a gap with zero or negligible states that falls between the VB and CB demonstrates the optoelectronic potential power of the system, which, as an important parameter, is defined as the band gap. Mg_3PCl_3 is known to have a wider band gap than Mg_3PBr_3. As a pattern in their band structures, the band gap decreases with the increasing atomic size of the halide from Cl to Br. This phenomenon is resulted due to the increased strength in electronegativity of chlorine which increases the ionic character of the bonds thus widening the band gap. Furthermore, the peaks of lesser sharpness in valence and conduction bands serve as evidence of attributed electronic states localized sharply signifying the potential effect on carrier mobility alongside the optical properties of the DOS plots.

The states located closer to the upper and lower limits of the band in Mg_3PBr_3 have better carrier connectivity when placed against Mg_3PCl_3. Due to this, Mg_3PBr_3 is better suited for high-performance applications like transistors and photodetectors. Therefore, the DOS analyses for the two compounds verify their distinguishing features as being semiconductor in nature as well as showcase the degree of impact the selection of halide has on the electrical properties of these compounds. These findings form the basis of how these materials should be processed as well as incorporated into various optoelectronic devices including solar cells, LEDs, and sensors where

Table 3 Calculated bandgap with different functional of the compound Mg_3PX_3 (X = Cl and Br)

	Band gap, E_g (eV)					
				Hybrid-HSE06		
Compound	GGA-PBE	GGA-WC	GGA-PBEsol	This work	Previous work	Reference no.
Mg_3PCl_3	2.297	2.289	2.258	3.093	3.21	29
Mg_3PBr_3	1.506	0.718	0.693	2.187	2.22	29

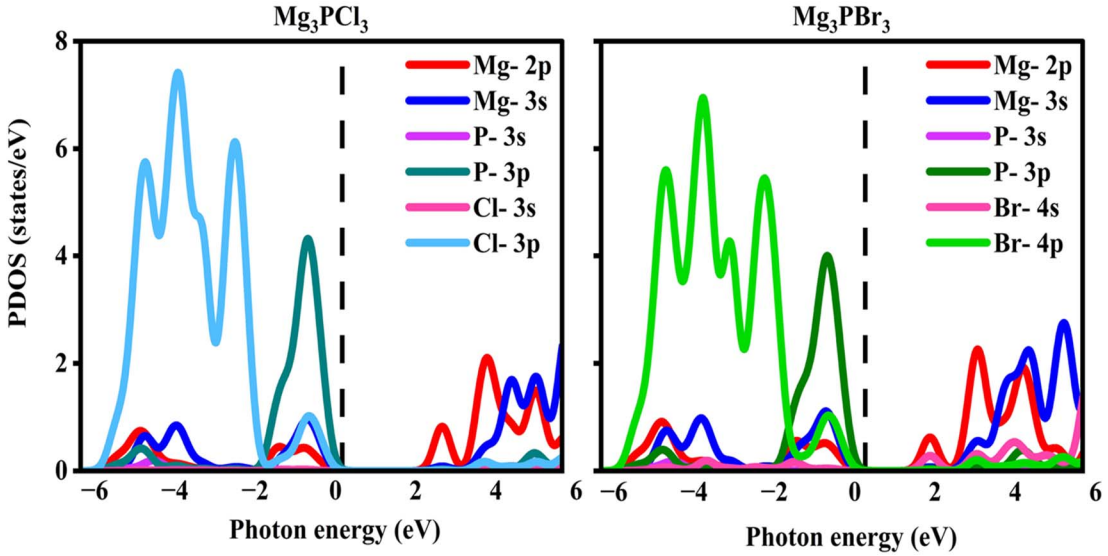

Fig. 6 Partial density of states of Mg_3PX_3 (X = Cl and Br).

regulation and control of band gap as well as motion of charge carriers is highly important. Once again, the comparison of Mg_3PCl_3 and Mg_3PBr_3 sheds light on the interrelations of the properties of halides including the magnitude of their electronegativity and size and the ability for the materialization of new technological devices.

Fig. 7 shows the structural or electronic configuration of a specific component of a Mg_3PX_3 (X = Cl and Br) with the arrangement of the Mg and (P) atoms in proximity exhibiting a periodic lattice characteristic of a Perovskite-like structure. The numbers (6.798×10^{-1}, 5.287×10^{-1}) correlate with the electron density contours, bond length, or atomic distances that explain the stability and the electrical properties of the structure material. The pattern created by the Mg and P atom's crystal structure with the fluctuation in values indicates non-homogeneous electron density.

This elusive bond provides crucial features such as conductive capabilities, the band gap, and optical behaviors, making the material might be useful in various fields such as solar cells and LEDs. Thermodynamic stability and mechanical stamina may very well be enhanced by using P instead of those flowing, energetic perovskites. These higher regions of free electrons hint at stronger bonds or localized electron states, while weak interactions suggest enduring voids as opposed to weak lattices containing stronger bonds. To enable robust electronic components and high-efficiency photovoltaic devices with real-world practicality, these details are important for optimizing the material's performance. The image broadens the simple knowledge posited of material science in a more fundamental atomistic understanding as a base for further computational studies to develop next-generation optoelectronic materials. By studying the bond patterns and electron cloud distribution, scientists can optimize compounds to give the desired response when subjected to external pressure or heat, enabling them to make materials with more functionality and greater stability. This structural analysis not only highlights the potential of

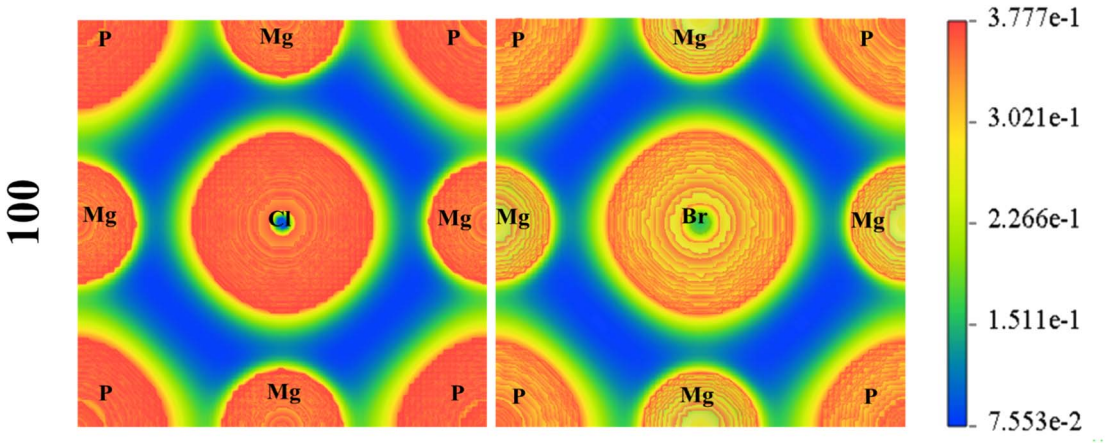

Fig. 7 Charge density mapping of Mg_3PX_3 (X = Cl and Br).

Mg_3PX_3 (X = Cl and Br) for advanced applications but also contributes to the broader field of perovskite research, offering insights into the role of different elements in shaping material properties.

3.3 Magnetic properties

Magnetic property describes the response of a material after applying a magnetic field effect.[46] This behavior is associated with interactions of electrons, spin in the orbital, and most importantly spin motion. Generally, the upward spin of electrons in the orbital is termed as α and the downward spin is denoted as β.[47] The electronic states and motion that confirm the magnetic behavior of compound Mg_3PX_3 (X = Cl and Br) are examined with the PDOS graph of the compound. To measure the response of the applied magnetic field, in CASTEP the "spin polarization" is changed in this calculation. It was taken "Co-linear" to study this behavior. From Fig. 8, the graph represents PDOS in the *Y*-axis from −6 to +6 eV per states and in the *X*-axis energy from −20 to +20 eV region. In the graph, the upward spin moments are exactly opposite to the downward moment, and that cancels out the whole momentum of the compound.[48] The α lines stayed in the positive region whereas in the negative region, the β lines are located. And they superimposed with one another, exhibit a perfect reflection of the α lines in the negative region which is denoted by β. As the neat momentum is zero then there is no magnetism occurring in the response of the applied magnetic field. When the upward spin momentum of the material is nullified by the downward spin, this characteristic is called Diamagnetism.[49] So, it follows that this material is diamagnetic and this behavior is not affected by the halogen replacement. As the bigger halogen is replaced in the structure the crystal lattice does not exhibit any kind of fluctuation from the diamagnetic nature. Both Mg_3PCl_3 and Mg_3PBr_3 show diamagnetic behavior and no noticeable changes occurred after changing the X site from Cl to Br. This diamagnetic nature makes this compound can be a superior candidate in magnetic sensors and shielding as well. Also, in the quantum mechanical sector, it can be used as an alternative.[50]

3.4 Optical properties

This study explores the effects of photon energy and the interaction of halide change on the compound Mg_3PX_3 (where X = Cl and Br). Calculations of the optical characteristics of Mg_3PX_3 (where X = Cl and Br) at photon energies of 30 eV show how the material's optical characteristics vary with different halides.

3.4.1 Absorption. Optoelectronic application performance evaluation heavily relies on optical absorption coefficient measurements because light absorption efficiency decides the efficiency of materials used in solar cells.[51] Mg_3PX_3 (X = Cl and Br) 's optical absorption properties became evident through measurements of the absorption coefficient values (α) against photon energy. The absorption spectra display optical activity through 0 to 30 eV photon range, reaching peak intensities at the 10^5 cm^{-1} level in Fig. 9(a).

The absorption spectra for both Mg_3PX_3 (X = Cl and Br) compounds show equivalent absorption characteristics that reach their highest point between 2.0×10^5 cm^{-1} to 3.0×10^5 cm^{-1}. Peak positions along with absorption strength distinguish these two compounds from one another. The peak absorption coefficient of Mg_3PCl_3 exceeds that of Mg_3PBr_3 because it reaches approximately 2.8×10^5 cm^{-1} while Mg_3PBr_3 peaks at around 2.6×10^5 cm^{-1}. Mg_3PBr_3 starts absorbing light at higher photon energy than Mg_3PCl_3 indicating that the absorption edge shows a redshift. The expansion of the ionic radius together with the reduced electronegativity forces of bromine lowers bandgap energy while promoting photon absorption at lower energies in the spectrum. The electronic band structures differentiate the way the two halides absorb light energy. The redshifted bandgap spectrum of Mg_3PBr_3 improves photon absorption throughout the visible

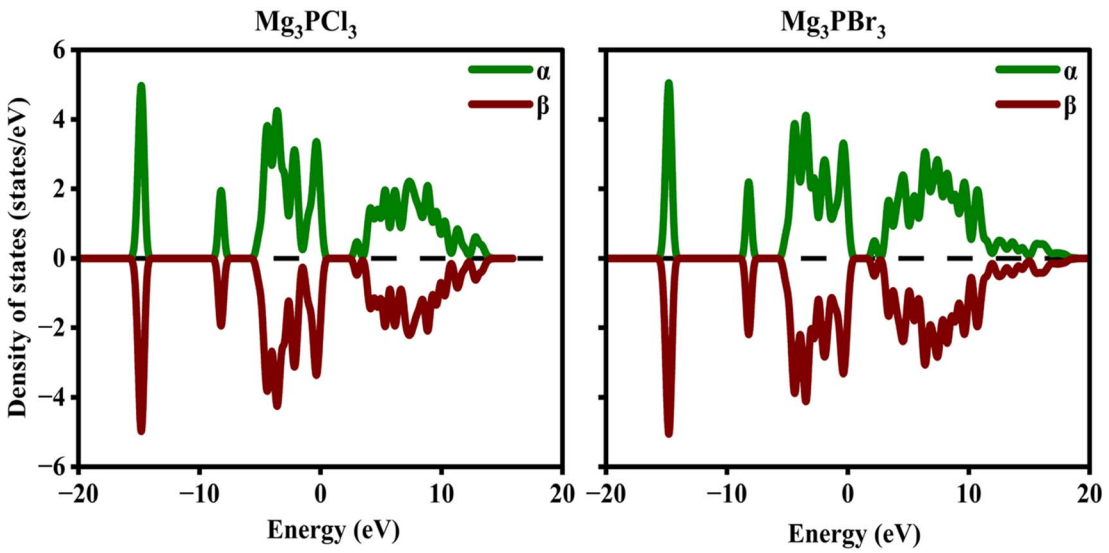

Fig. 8 Magnetic PDOS of Mg_3PX_3 (X = Cl and Br).

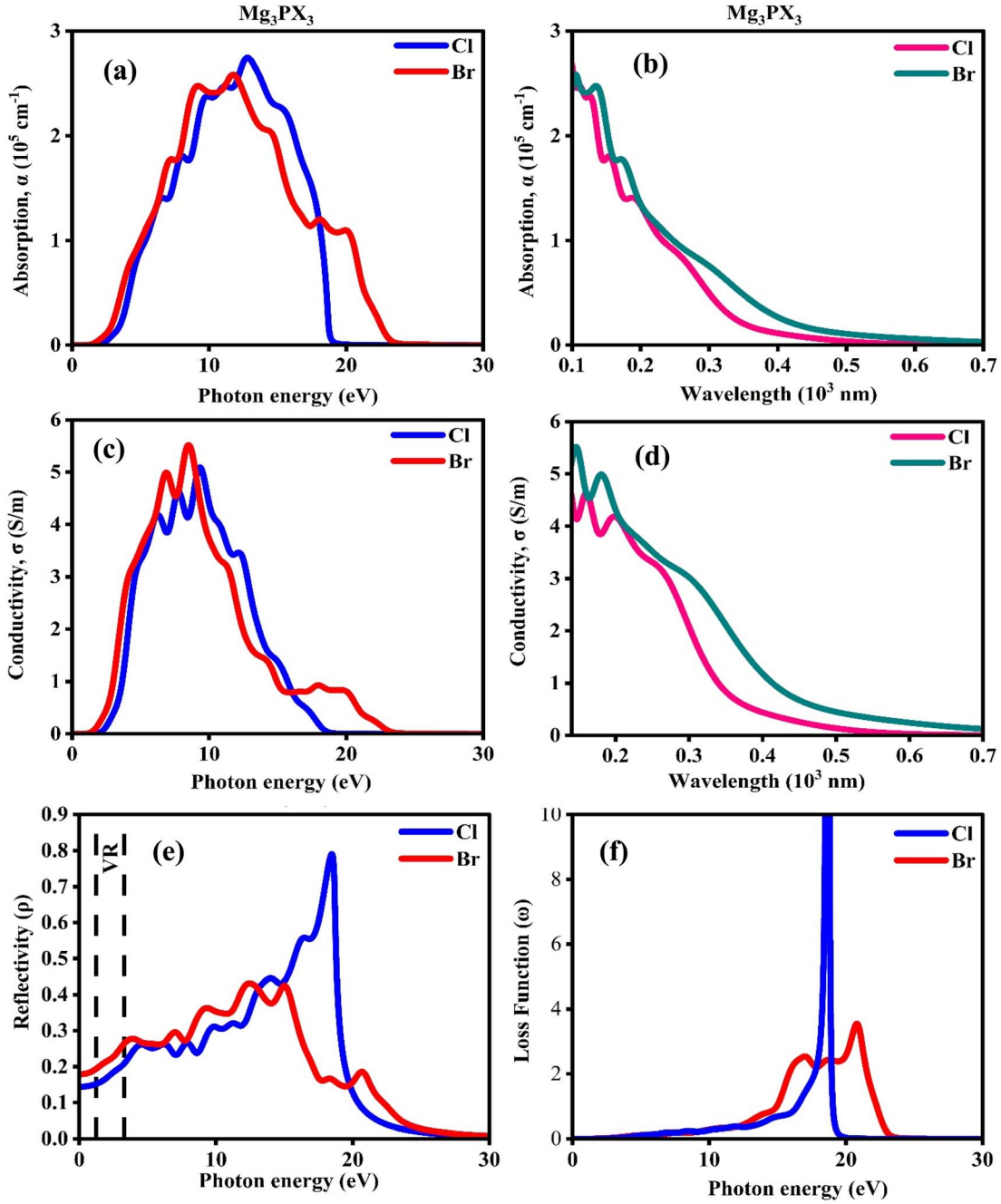

Fig. 9 Calculated (a) absorption *vs.* energy (b) absorption *vs.* wavelength, (c) conductivity *vs.* energy, (d) conductivity *vs.* wavelength (e) reflectivity, and (f) loss function of Mg_3PX_3 (X = Cl and Br).

wavelengths. The red edge effect in Mg_3PBr_3 enhances its suitability for optoelectronic applications requiring expanded energy reach because it is a candidate in solar cell and device development. Lower energy light interacts more effectively with Mg_3PCl_3 crystals because of its elevated absorption coefficient; thus, this material might be an appropriate alternative for high-efficiency photodetector and UV protective applications. Fig. 14, shows the wavelength *vs.* absorption spectra where the highest absorption is found between 100–300 nm range of wavelength and the absorption coefficient is around 2.8×10^5 cm^{-1} range which indicates the absorption in the UV region. In addition to the energy band gap, the absorption coefficient and its relation to wavelength play a crucial role in determining the suitability of materials for photodetector and UV protective applications. A strong absorption coefficient in the UV and visible range enhances a material's efficiency in such applications. Snaith *et al.*[52] demonstrated this range of absorption can be appropriate for detectors. Rony *et al.*[31] studied $TlBX_3$ (B = Ge, Sn; X = Cl, Br, I) and found the highest absorption spectra in the UV range as compared to this study and predicted they can be used

in photodetector as the major peaks are in the UV region. A high refractive index in the UV range enhances light–matter interaction, which is crucial for photodetector efficiency.[53] The data calculated from the refractive index ensures this finding and enhances the probabilities of the prediction of the materials that can be used as photodetectors. The imaginary part of the dielectric function (ε_2) also cross-checks these findings with a greater ε_2 at the UV region which is discussed in the upcoming sections.

3.4.2 Conductivity. Fig. 9(b) shows the electrical conductivity $\sigma(\omega)$ of Mg_3PX_3 (X = Cl and Br) which exhibits the material's sensitivity to photon energy. In this regard, the parameter of the first category is related to the dielectric constant and its representation as the measure of the dielectric constant to the electric current when the material is illuminated and calculated using eqn (3).

$$\sigma(\omega) = \frac{\alpha(\omega)n(\omega)c}{4\pi} \tag{3}$$

The wide conductivity spectrum indicates that both compounds achieve maximum values between 5.0–5.5 S m^{-1} thereby demonstrating their suitability for electronic and optoelectronic applications. The conductivity measurements of Mg_3PCl_3 and Mg_3PBr_3 show both comparable trends and distinguishing characteristics regarding peak performance. Mg_3PBr_3 achieves the highest conductivity peak value of 5.4 S m^{-1} yet Mg_3PCl_3 reaches 5.1 S m^{-1} as its peak value. The charge transport mechanisms in Mg_3PCl_3 are extended longer than those of Mg_3PBr_3 while the range of operation is broader. Mg_3PBr_3 starts conducting at lower energies because its charge transportation activation energy remains lower than that of Mg_3PCl_3. Bromine provides increased delocalization to the electron cloud because its larger ionic radius and lower electronegativity properties lead to better charge mobility. Mg_3PBr_3 attains better peak conductivity levels than Mg_3PCl_3 but its conductivity values decrease faster with rising energy than the slower fading performance of Mg_3PCl_3 across the energy range. The comparatively stable charge transport capabilities of Mg_3PCl_3 position it as a suitable material for long-term field-effect transistors (FETs), sensors, and photodetectors applications. Mg_3PBr_3 shows advantageous peak conductivity values which enable its use in high-frequency electronic devices along with charge-storage applications because it ensures swift charge transfer processes. The optical conductivity characteristics of Mg_3PBr_3 improved further because it combined its redshifted absorption edge with a wider absorption range in the visible part of the spectrum. Mg_3PBr_3 shows promising performance characteristics for photovoltaics and photodetectors because its increased conductivity matches its redshifted absorption properties. Mg_3PCl_3's wider conductivity range, coupled with high absorption capability, makes it a suitable candidate for both long-lasting optoelectronic device applications and might be used in UV-detecting materials.

3.4.3 Reflectivity. The reflectivity spectrum $R(\omega)$ for Mg_3PX_3 (X = Cl and Br) shown in Fig. 9(c) would be useful in understanding the optical nature of the compound and measured implementing eqn (4).

$$R(\omega) = \frac{(n-1)^2 + k^2}{(n+1)^2 + k^2} \tag{4}$$

The reflectivity spectra (ρ) measured against photon energy show different optical characteristics between the two compounds. The optical properties of Mg_3PCl_3 show greater reflectivity reaching 0.78 at 20.5 eV photon energy than the reflectivity of 0.58 at 18 eV for Mg_3PBr_3. The reflectance peak in Mg_3PCl_3 appears sharp causing stronger light reflectance in the ultraviolet (UV) spectrum which proves its capability to function as a UV reflection material. The broad and weak absorption peak of Mg_3PBr_3 matches its previously recorded absorption energy shift together with its reduced photon energy values. The visible spectrum (VR) shows moderate reflectivity effectiveness between the two compounds where Mg_3PCl_3 produces slightly higher reflectivity values than Mg_3PBr_3. Mg_3PCl_3 demonstrates better reflectivity due to its higher absorption coefficient as well as its sharp photon peak thus addressing opportunities in high-energy optical coatings, UV reflectors, and photonic devices.[54] The wide spectral reflectivity area of Mg_3PBr_3 makes it suitable for applications where broad spectral response is needed including solar energy harvesting, optical sensors along anti-reflective coatings. The photodetectors and photovoltaic cells benefit from increased light–matter interaction because of the declining reflectivity pattern beyond peak regions in both materials. The substitution of halogens controls how optics behave in distinct ways since chlorine creates stronger UV protection along with improved reflectivity and bromine generates broader spectral wavelength capabilities with increased visible light absorption. Studies demonstrate how Mg_3PX_3 (X = Cl and Br) compounds allow reflectivity customization for unique applications thus establishing them as future optical coating and window and mirror technology candidates. The adjustment of optical properties by altering halide composition unlocks various potential uses for advancing optics together with producing unique solutions for different industrial applications.

3.4.4 Loss function. The loss function $L(\omega)$ of Mg_3PX_3 (X = Cl and Br) which identifies the energy losses when an electron travels through the material is analyzed in Fig. 9(d) and calculated using eqn (5). The loss function defines how electrons lose energy through external electromagnetic field interactions thus it establishes fundamental knowledge about dielectric responses.[55]

$$L(\omega) = \frac{\varepsilon_2(\omega)}{{\varepsilon_1}^2(\omega) + {\varepsilon_2}^2(\omega)} \tag{5}$$

The collective electron oscillation peaks of Mg_3PCl_3 and Mg_3PBr_3 appear differently in terms of position and strength. The main photon peak of Mg_3PCl_3 occurs at 20.5 eV where it reaches a maximum value of 10 indicating intense collective electron motions which produce substantial energy loss at that

frequency. The photon interaction strength in Mg_3PBr_3 is lower compared to other materials since its principal loss peak at 18 eV serves as a broad and less intense resonance. Mg_3PBr_3 displays numerous smaller absorption peaks below 15 eV thus indicating interband transitions which are more complex than in Mg_3PCl_3. The higher photon energy of Mg_3PCl_3 indicates it possesses both a larger bandgap structure and stronger electronic binding forces that resulted in previously observed enhancements of absorption coefficient and high conductivity range. Lower photon energy in Mg_3PBr_3 matches up with both its shifted absorption spectrum in the red direction and its improved charge mobility characteristics because of greater electron delocalization and reduced requests for excitation energy. Physical observations suggest that Mg_3PCl_3 shows promise as both a deep UV photon device and high-frequency optoelectronic element, and Mg_3PBr_3 demonstrates suitability for visible-light photon applications as well as sensing needs and energy collection applications. The dissimilar outcomes regarding energy loss between the two halide forms indicate that Mg_3PX_3 (X = Cl and Br) materials open a wider area of application and can be promising prospects for dielectric coatings as well as transparent conductive materials and advanced photon nanostructures.

3.4.5 Dielectric functions. The complex dielectric function is represented as eqn (6),

$$\varepsilon(\omega) = \varepsilon_1(\omega) + i\varepsilon_2(\omega) \tag{6}$$

Optoelectronic devices depend heavily on the dielectric function to determine their efficiency and performance levels.[56] Fig. 10(a) displays the real part of the dielectric function $\varepsilon(\omega)$ for Mg_3PX_3 (X = Cl and Br) as it depicts how the materials respond to electromagnetic fields by storing electric energy. Mg_3PBr_3 attains its highest value of 8.5 F m^{-1} within its photon energy curve but Mg_3PCl_3 achieves just slightly lower at 7 F m^{-1}. The dielectric strength of Mg_3PBr_3 reaches higher levels compared to other test materials which indicates superior static dielectric constant capability. The transition from dielectric to metallic response in both materials becomes noticeable as photon energy rises because they both show a strong reduction in $\varepsilon(\omega)$ until reaching zero and establishing photon behavior. The $\varepsilon(\omega) = 0$ threshold occurs at lower frequencies in Mg_3PBr_3 while supporting its previously documented tendency of redshifted optical properties and lower photon energy. The behavior of both materials features minor variations before stabilizing at zero energy levels when energy reaches higher values. The $\varepsilon(\omega)$ response indicates Mg_3PBr_3 would excel at capacitive power storage and electronic devices and solar cell layers but Mg_3PCl_3 offers superior performance in optical and photon device applications.

The dielectric properties offer a fundamental understanding of optical wave–material interactions which prepares the basis for evaluating both energy dissipation and absorption behaviors using the imaginary part of the dielectric function. Mg_3PCl_3 shows a significant absorption peak near 8 eV, and Mg_3PBr_3 also shows a similar peak; however, it's at approximately 7 eV, and this lower energy peak is interesting which is shown in Fig. 10(b). This downward shift is because of Br's heavier mass compared to Cl's, resulting in weaker bonding, and subsequently, less energy is required for electron movement. Moreover, the peak sizes differ, and this suggests variations in electron movement. These findings demonstrate that we can easily adjust the optical properties of these materials by changing the halide, and this gives us options for making light devices that operate in different spectral regions.[57] This ability is further aided by changing halides and altering optical properties, leading to easier production and implementation.[58]

3.4.6 Refractive index. The refractive index $n(\omega)$ for Mg_3PX_3 (X = Cl and Br) provides information concerning the light–matter interaction and analyses of its optical properties and proposed technological uses. The refractive index related to the real part of the dielectric function reveals the impact upon light phase velocity and polarizability using eqn (7).[59]

$$n(\omega) = \left[\frac{\left\{\sqrt{\varepsilon_1{}^2(\omega) + \varepsilon_2{}^2(\omega)}\right\} - \varepsilon_1(\omega)}{2}\right]^{\frac{1}{2}} \tag{7}$$

Fig. 10(c) reveals the optical dispersion characteristics of materials by showing Mg_3PX_3 (X = Cl and Br) refractive index against photon energy $n(\omega)$ behavior. The refractive index for Mg_3PCl_3 and Mg_3PBr_3 starts at a high initial value when the photon energy is low yet Mg_3PBr_3 reaches this peak value first before Mg_3PCl_3 which indicates more robust light interaction and slower phase velocity within that range. Photon energy rise leads to multiple oscillations in both materials which match interband transition patterns together with decreasing refractive index values. The observed intensity patterns in the refractive index fit with dielectric function measurements, which show that Mg_3PBr_3 provides stronger optical responses in lower-energy regions compared to Mg_3PCl_3 when demonstrating higher refractive index stability at elevated photon frequencies. Using higher photon energies, both materials display decreased optical refraction, which makes them valuable for high-energy optics, antireflective coatings, and tunable refractive index materials for photonic devices. The variations in the refractive index demonstrate that Mg_3PBr_3 fits visible and near-infrared operating spectra better than Mg_3PCl_3, which excels at UV and high-energy optical systems. The refractive index behavior demonstrates it can be suitable for energy applications together with optical sensor design because accurate refractive index control is essential. Further understanding of material optical behavior stems from analyzing $n(\omega)$'s dispersion characteristics since $\varepsilon_2(\omega)$ enables absorption loss and energy dissipation analysis.

A photon energy spectrum shows distinctive dispersion characteristics in the refractive index $n(\omega)$ measurements of Mg_3PX_3 (X = Cl and Br) materials according to Fig. 10(d). The high refractive index values observed in Mg_3PCl_3 and Mg_3PBr_3 operate at lower photon energy points while the peak value of Mg_3PBr_3 stands above Mg_3PCl_3 showing superior light confinement abilities and slower phase velocity response. The optical refraction decreases while photon energy rises, causing

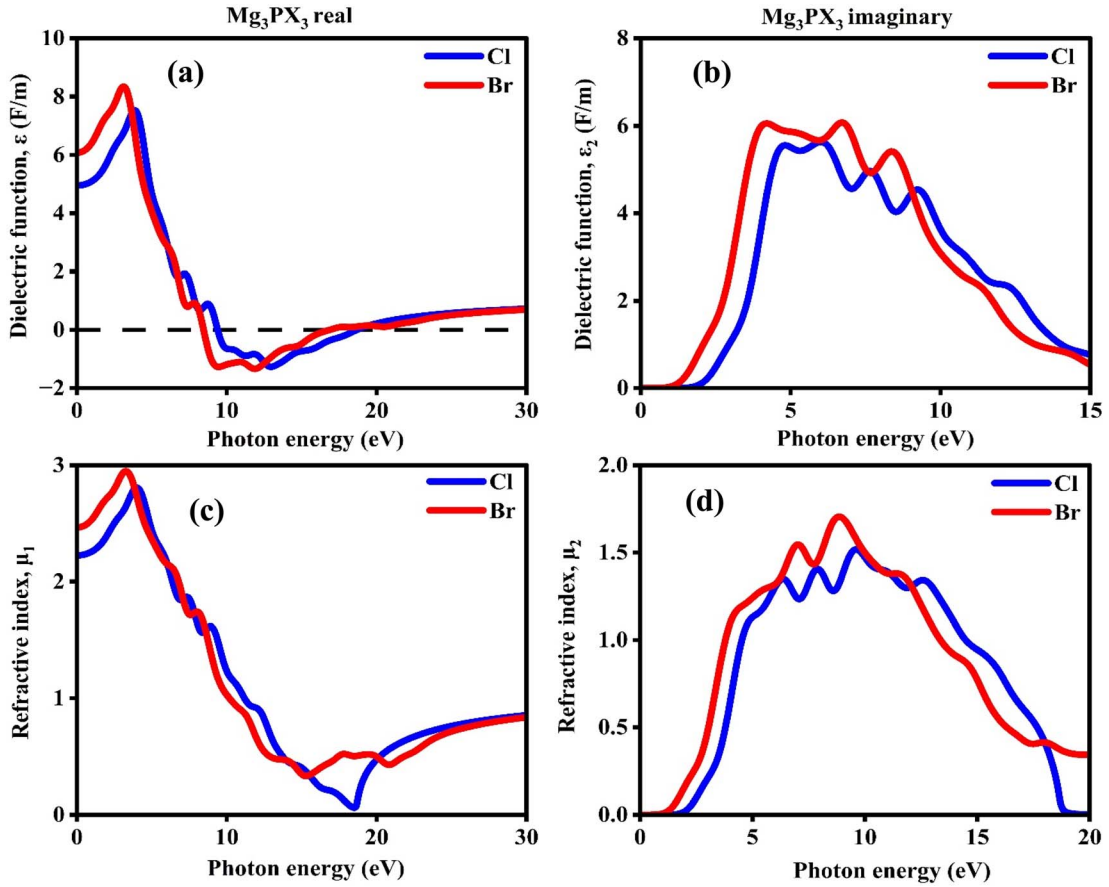

Fig. 10 Calculated (a) dielectric function (real), (b) dielectric function (imaginary), (c) refractive index (real), and (d) refractive index (imaginary) of Mg_3PX_3 (X = Cl and Br).

$n(\omega)$ to diminish.[60] Two primary inter-band electronic transitions appear in both curves, but Mg_3PCl_3 demonstrates faster decreasing refractive response patterns after 10 eV compared to Mg_3PBr_3, displaying a broader refractive spectrum response. Both Mg_3PBr_3 perform better for visible and infrared optical needs, but Mg_3PCl_3 opens the door of very much suitable for UV-based applications and high-energy optical coating requirements. The observed refractive index patterns demonstrate suitable properties for building photon guides together with optoelectronic devices as well as photonic materials that need adjustable optical properties. The study of optical response and energy dissipation requires analysis of the imaginary part of the dielectric function $\varepsilon_2(\omega)$ because this quantity represents both absorption characteristics and photon energy loss in materials.

3.5 Mechanical properties

This characteristic primarily indicates how a material will respond to different applied pressures and loads.[61] Since it is impractical to investigate an unstable construction, mechanical stability is an essential criterion. In Table 4, three independent parameters, referred to as C_{11}, C_{12}, and C_{44} present three different specifications of a material. C_{11} shows the stiffness of a material when the load is applied in one direction. C_{12} shows the coupled stress, and C_{44} shows the shear deformation resistive nature.[62] Then, the stability requirement of Born's rule, $C_{11} - C_{12} > 0$, $C_{11} + 2C_{12} > 0$, and $C_{44} > 0$.[63] Mg_3PCl_3 has the largest elastic constant, C_{11}. Table 4 fulfills the Born stability requirements and can consider this compound Mg_3PX_3 (X = Cl and Br) as a mechanically stable compound. As the halogen is changed, there is a slight change in every parameter, but still, they are stable.

The physical phenomena whether a material is stiff or ductile can be calculated from this calculation. All the mechanical characteristics will be concluded from this calculation. Some parameters are included in this study such as shear modulus (B), bulk modulus (G), elastic modulus (E), Poisson's ratio (ν), and Paugh's ratio, *etc.* Each parameter can be calculated from the formula as follows:[64]

Table 4 Calculated elastic constant of the compound Mg_3PX_3 (X = Cl and Br)

Compound	C_{11} (GPa)	C_{12} (GPa)	C_{44} (GPa)	C_{12}–C_{44} (GPa)
Mg_3PCl_3	86.90	20.02	34.41	−14.39
Mg_3PBr_3	86.74	27.98	30.07	−2.09

$$\text{Bulk modulus, } B = \frac{C_{11} + 2C_{12}}{3} \quad (8)$$

$$\text{Shear modulus, } G = \tfrac{1}{5}(C_{11} + C_{12} - 3C_{44}) \quad (9)$$

$$\text{Young's modulus, } E = \frac{9BG}{3B + G} \quad (10)$$

$$\text{Poisson's ratio, } \nu = \frac{3B - E}{6B} \quad (11)$$

$$\text{Vicker's hardness, } H_V = \frac{(1 - 2\nu)E}{6(1 + \nu)} \quad (12)$$

$$\text{Machinability index, } \mu_m = \frac{B}{C_{44}} \quad (13)$$

$$\text{Paugh's ratio} = \frac{B}{G} \quad (14)$$

The spinodal requirement that is equivalent to bulk modulus (B) is another benchmark to be regarded as mechanically stable.[65] From Table 5, the bulk modulus is positive which recommends this is mechanically stable. Bulk modulus has another significance, it is the property of a material that denotes the resistance to fracture.[67] Mg_3PBr_3 has the largest bulk modulus of 47.57 GPa among them, so it shows more resistance than Mg_3PCl_3 which has 42.32 GPa, when fracture occurs. Low bulk modulus also represents softness.

C_{12}–C_{44} represents the Cauchy pressure of a material. It is a crucial parameter for a compound to determine the ductile/brittle nature of a compound. If the Cauchy pressure is positive, it implies the compound is ductile and the negative value declares the brittleness.[68] The outcome of this computation is shown in Table 4 and the Cauchy pressure is found consistently negative for both of them. It represents the stiff nature of the compound. Mg_3PCl_3 is more brittle than Mg_3PBr_3 with a more negative value of −14.39 GPa. Heavier halogen substitution lowers the brittleness of the compound in Cauchy pressure calculation. A recent study by Rahman *et al.*[66] on Mg_3PF_3 shows a similar kind of negative Cauchy pressure which validates the findings of this study. From Table 5, when the halogen is replaced from Cl to Br, the bulk, shear, and elastic modulus decrease. It is evident from Table 5 that, the bulk, Young's, and shear modulus of chloride photovoltaic perovskite is superior to Mg_3PBr_3 in this computation. High bulk modulus makes this compound well-suitable in construction sectors, and pressure vessels in which high-strength materials are needed without deformation.[69] The shear modulus G is a parameter that indicates the ability to resist deformation on loading. In this research, both materials exhibit higher shear with a value of 34.02 GPa for Mg_3PCl_3 and 29.80 GPa for Mg_3PBr_3 and that denotes higher plastic deformation ability of the compound. There are other parameters to confirm the ductile/brittle nature of a compound such as Poisson's ratio (ν), and Paugh's ratio (B/G). There is a threshold magnitude of each parameter which confirms the phenomenon of the compound. For Poisson's ratio, If the compound has a greater Poisson's ratio than 0.26 it will be considered a ductile material and if the value is lower than this it is brittle.[70] Table 5 ensures that Mg_3PCl_3 and Mg_3PBr_3 both exhibit a brittle nature. Mg_3PCl_3 Is more brittle with a value of 0.183 and Mg_3PBr_3 is closer to the value of ductility with a magnitude of 0.240 visualized in Fig. 11. At the 1.75 value of Paugh's ratio, the conversion of brittle to ductile occurs. In this computation, the compound Mg_3PX_3, based on the information shown in Table 5, Mg_3PCl_3 has 1.24 and Mg_3PBr_3 has 1.60 which is less than the threshold and that is determining the brittle nature of the compound. These results cross-checked the findings of Cauchy pressure. This highly brittle nature makes this compound applicable in energy and shock absorber sectors.[71] This is shown graphically in Fig. 12. "μ_m" is known as the machinability index of a material. A high index of machinability indicates the soft, malleable nature of the material. In this particular research, this index is much lower. Mg_3PCl_3 has 1.23 and 1.58 for Mg_3PBr_3, and this is a much lower value. Based on this index, this material can't be easily shaped with higher friction and lower lubricity. The heavier halogen replacement makes this material softer in the study. Hardness measures a material's ability to maintain its shape under stress. Higher hardness shows more resistance to stress, and in this study, Mg_3PCl_3 has a hardness value of 8.72, and Mg_3PBr_3 has 5.98, which is much higher in general. As the higher hardness exhibits a much lower machinability index, the compound can be used in engineering tools and wear-resistant surface coatings.[72] Rahman *et al.*[66] studied a similar kind of compound Mg_3PF_3 and found comparable data shown in Table 5.

Table 5 Calculated mechanical properties of the compound Mg_3PX_3 (X = Cl and Br) with other reference work

Mechanical properties	Compound			
	This work		Reference work	
	Mg_3PCl_3	Mg_3PBr_3	Mg_3PF_3	Reference no.
B (GPa)	42.32	47.57	66.28	66
G (GPa)	34.02	29.80	43.60	66
E (GPa)	80.49	73.95	107.28	66
ν	0.183	0.240	0.23	66
$\frac{B}{G}$	1.24	1.60	1.52	66
μ_m	8.72	5.98	—	
H_v	1.23	1.58	—	

Anisotropy can be termed as a phenomenon of a material showing different properties in different directions.[73] The formulas to determine crystal anisotropy are mentioned below:

$$A_1 = \frac{4C_{44}}{C_{11} + C_{33} - 2C_{13}} \quad (15)$$

$$A_2 = \frac{4C_{55}}{C_{22} + C_{33} - 2C_{23}} \quad (16)$$

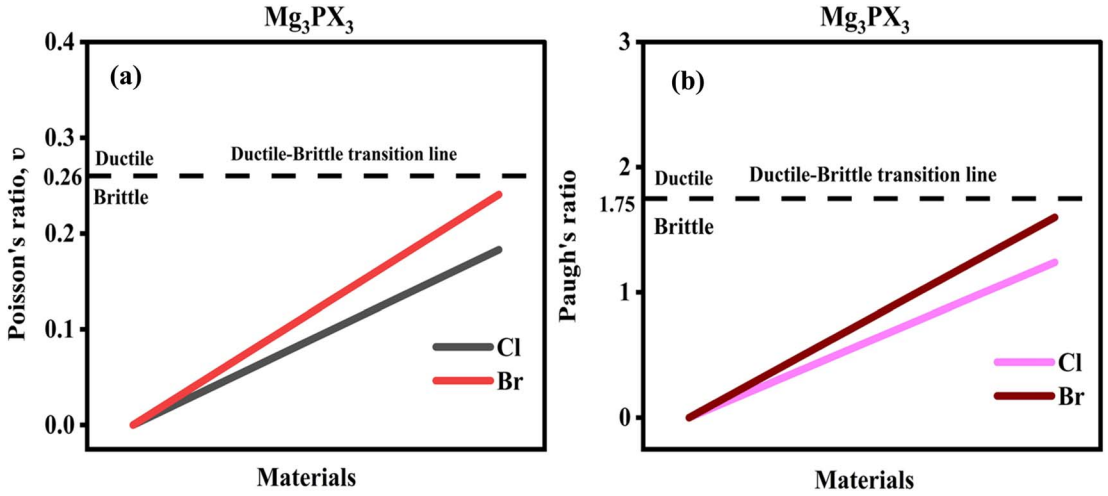

Fig. 11 (a) Paugh's ratio and (b) Poisson's ratio of Mg_3PX_3 (X = Cl and Br).

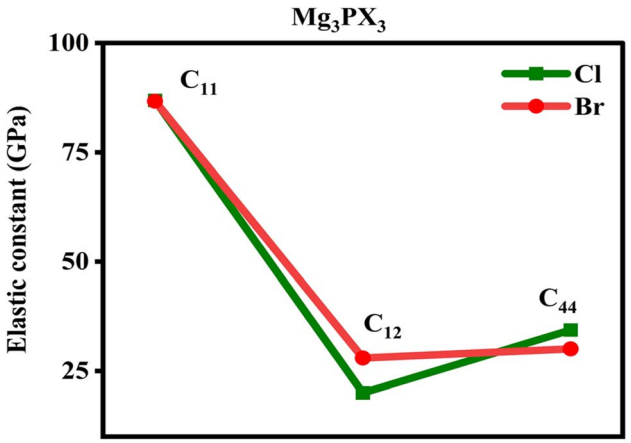

Fig. 12 Elastic constant of Mg_3PX_3 (X = Cl and Br).

$$A_3 = \frac{4C_{66}}{C_{11} + C_{22} - 2C_{12}} \tag{17}$$

For cubic symmetry,

$$A_1 = A_2 = A_3 = \frac{4C_{44}}{C_{11} + C_{33} - 2C_{13}} = \frac{2C_{44}}{C_{11} - C_{12}} \tag{18}$$

The Zener isotropic factor,

$$A = \frac{2C_{44}}{C_{11} - C_{12}} \tag{19}$$

To achieve isotropic behavior, the Zener factor is $A_1 = A_2 = A_3 = 1$, but in this study, this value is larger than 1; for Mg_3PCl_3, it is 1.029, and 1.023 for Mg_3PBr_3, which confirms the anisotropic nature of the compound.[74] Also, from the ELATE tool's 3D representation of Young, Poisson's, and shear moduli, the graphical output shows different types of structure in each spheroid case. The difference in the representation also confirms the anisotropic nature of the compound.[75] The ELATE graphical representations are presented in Fig. 13. And the 2D plots generated from ELATE of these moduli are also shown in Fig. 15, and 16.

3.6 Thermal properties

First-principle methods calculate thermal properties, which demonstrate the understanding of the act of a material acts when temperature changes. These properties include transverse velocity (V_t), longitudinal velocity (V_l), mean velocity (V_m), minimum thermal conductivity (K_{min}), lattice thermal conductivity (K_{ph}), Debye temperature (θ_D), and melting point (T_m). Table 6 shows the properties of the compounds Mg_3PCl_3 and Mg_3PBr_3, which have potential applications for high-temperature environments. Table 6 also represents the properties calculated by using the equations below.[76] Eqn (26) is an empirical equation:[77]

$$V_t = \sqrt{\frac{G}{\rho}} \tag{20}$$

$$V_l = \sqrt{\frac{3B + 4G}{3\rho}} \tag{21}$$

$$V_m = [\tfrac{1}{3}(2V_T^{-3} + V_L^{-3})]^{-\frac{1}{3}} \tag{22}$$

$$K_{min} = k_B V_m \left(\frac{M}{n\rho N_A}\right)^{-\frac{2}{3}} \tag{23}$$

$$K_{ph} = A\frac{M_{av}\theta_D{}^3\delta}{\gamma^2 n^{\frac{2}{3}} T} \tag{24}$$

$$\theta_D = \frac{h}{k_B} V_m \left[\frac{3n\rho N_A}{4\pi M}\right]^{\frac{1}{3}} \tag{25}$$

$$T_m = (554 + 5.911C_{11}) \pm 300\ \text{K} \tag{26}$$

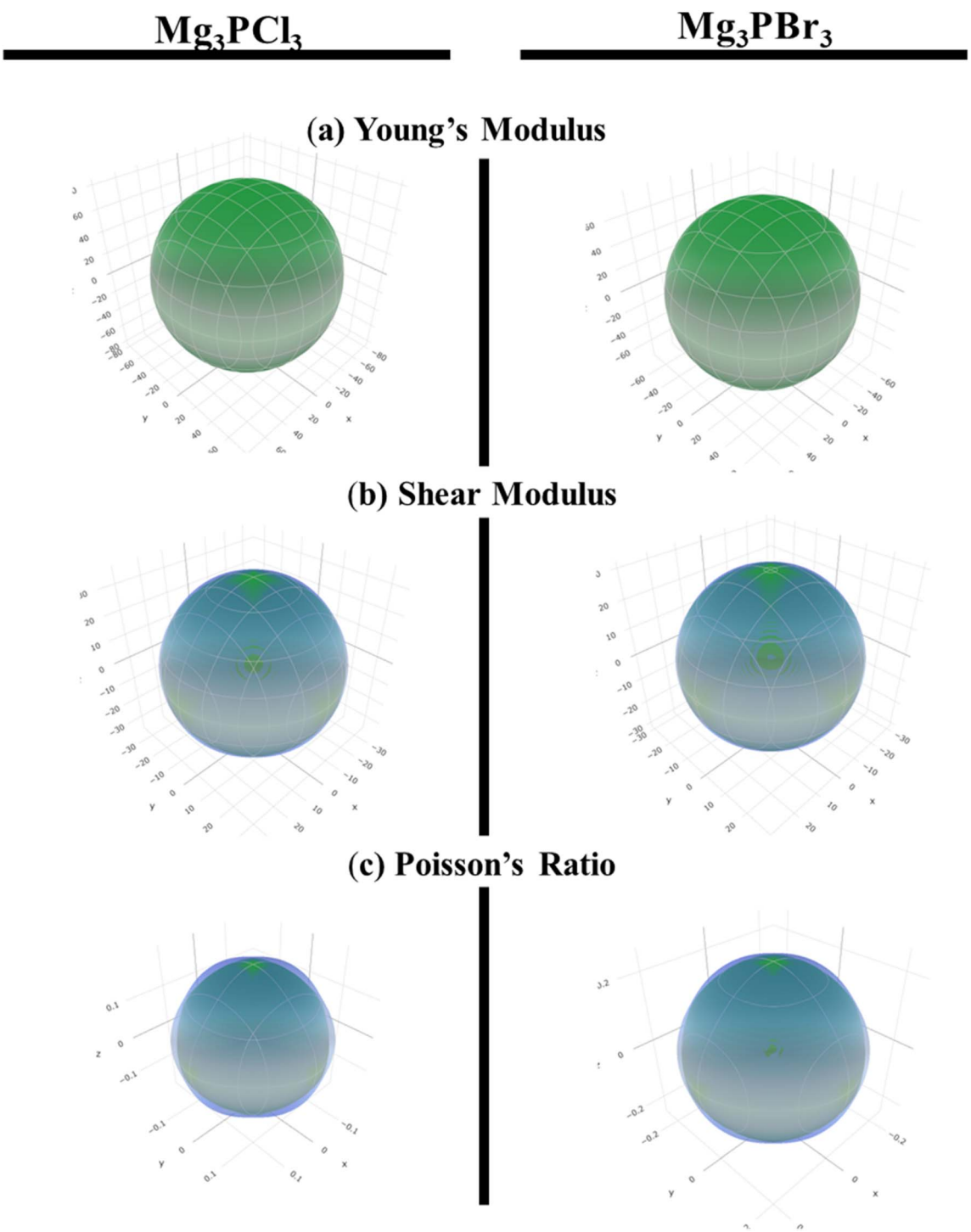

Fig. 13 The 3D illustration of (a) Young modulus, (b) shear modulus, and (c) Poisson ratio of Mg_3PX_3 (X = Cl and Br).

Transverse sound velocity (V_t) is the speed with which the transverse (shear) waves move through a material. Longitudinal sound velocity (V_l) suggests the velocity of propagations of the compressional or longitudinal waves. Transverse velocity is the velocity at which a wave material can travel perpendicular to the fibers, while longitudinal velocity is the velocity at which a wave material can travel along the fibers.[78] Therefore, V_m is the arithmetic average of the two velocities and gives an overall estimate of wave speed.[79]

For Mg_3PCl_3, the calculated value of V_t is 119 106.9 m s^{-1}, V_l is 458 543 m s^{-1} and V_m is 31 420.22 m s^{-1}. For the compound Mg_3PBr_3, the values of V_t, V_l, and V_m are 92 654.17 m s^{-1}, 550 426.2 m s^{-1}, and 24 493.77 m s^{-1}, respectively. The longitudinal sound velocities are much higher than the transverse velocities for both materials. The calculation shows that the V_t and V_m of

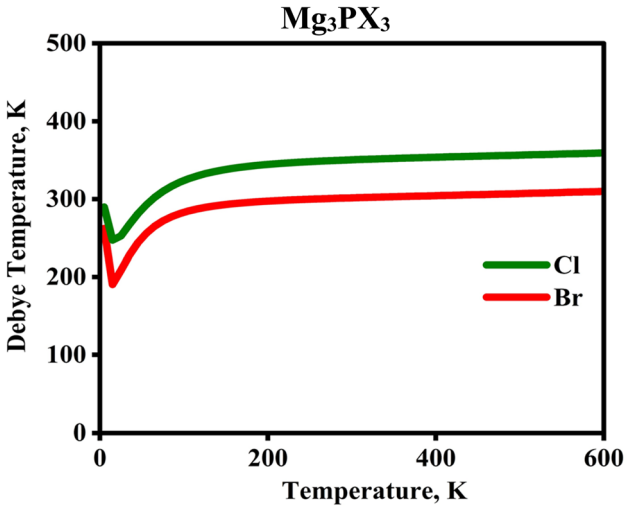

Fig. 14 Debye temperature of Mg_3PX_3 (X = Cl and Br).

Mg_3PCl_3 is higher than that of which means that the acoustic wave transmission in the material and thus it may be stiffer than that of Mg_3PBr_3. Also, Mg_3PBr_3 has a higher longitudinal velocity which implies that the material transmits longitudinal waves more effectively. V_m is essential to determine other thermal parameters for thermal conductivity. Mg_3PCl_3 demonstrates greater V_m with improved collective oscillations of lattice vibrations that relate well with enhanced mechanical strength and efficient heat conduction. All of these sound velocities are correlated with the material's elastic constants and its mechanical behavior. Higher velocities also mean a stiffer and more robust material and hence is capable of withstanding mechanical and thermal stresses. Thus, in terms of heat transfer or vibration damping requirements, Mg_3PCl_3 would be preferred because of its more or less balanced acoustic characteristics.

Lattice thermal conductivity (K_{ph}) is a heat transport property that defines how well a material supports the passage of heat by lattice vibrations.[80] Minimum thermal conductivity (K_{min}) is thermal conductivity at the lowest, restricted by the atomic structure and density of the material.[81] The compound Mg_3PCl_3 shows the K_{ph} value of 50.9857 W m^{-1} K^{-1} and K_{min} value is 0.0459 W m^{-1} K^{-1} while in the case of Mg_3PBr_3 the values of K_{ph} at 20.95515 W m^{-1} K^{-1} and K_{min} at 0.05015 W m^{-1} K^{-1}. Both K_{ph} for the compounds are significantly higher than

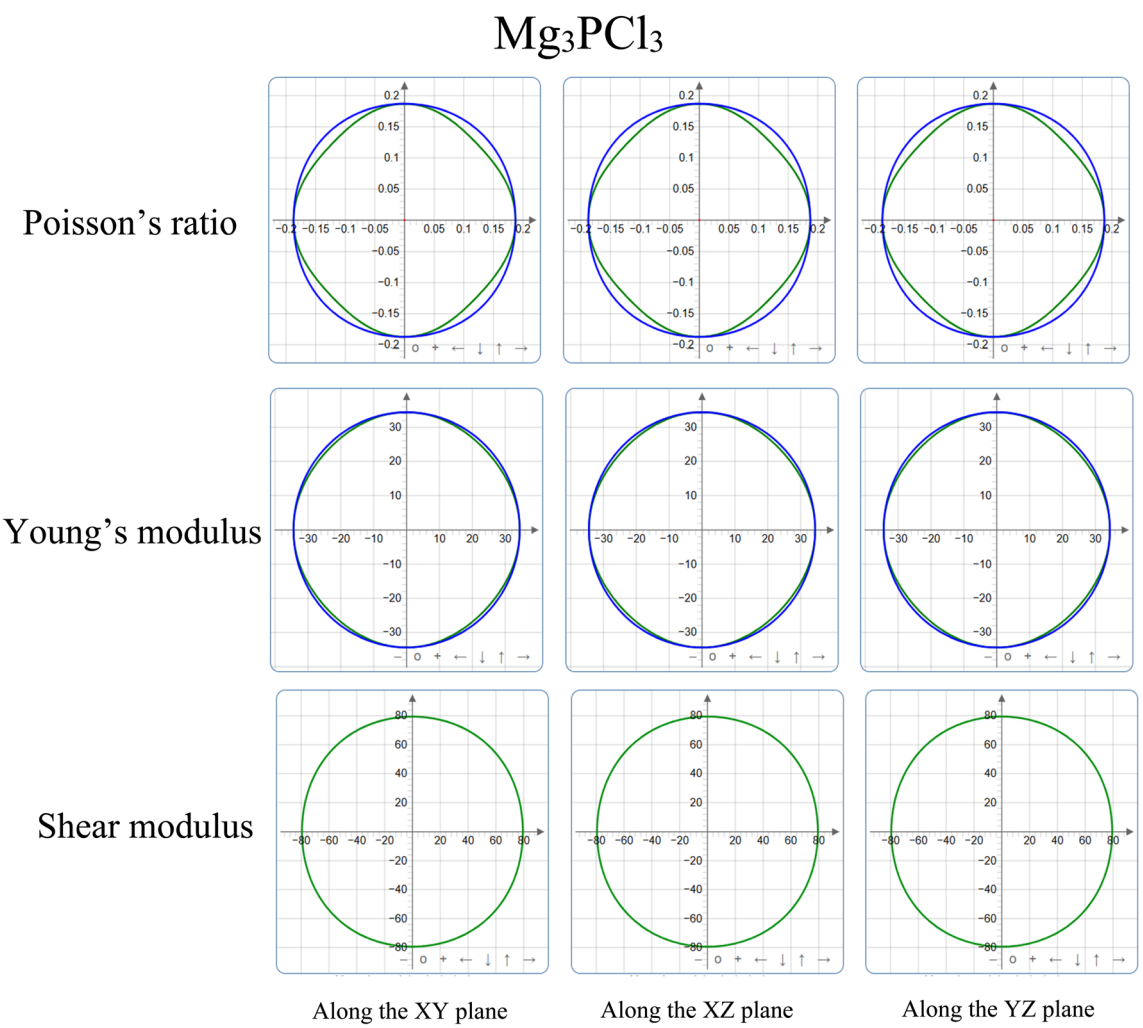

Fig. 15 The 2D illustration of Poisson ratio, Young modulus, and shear modulus of Mg_3PCl_3.

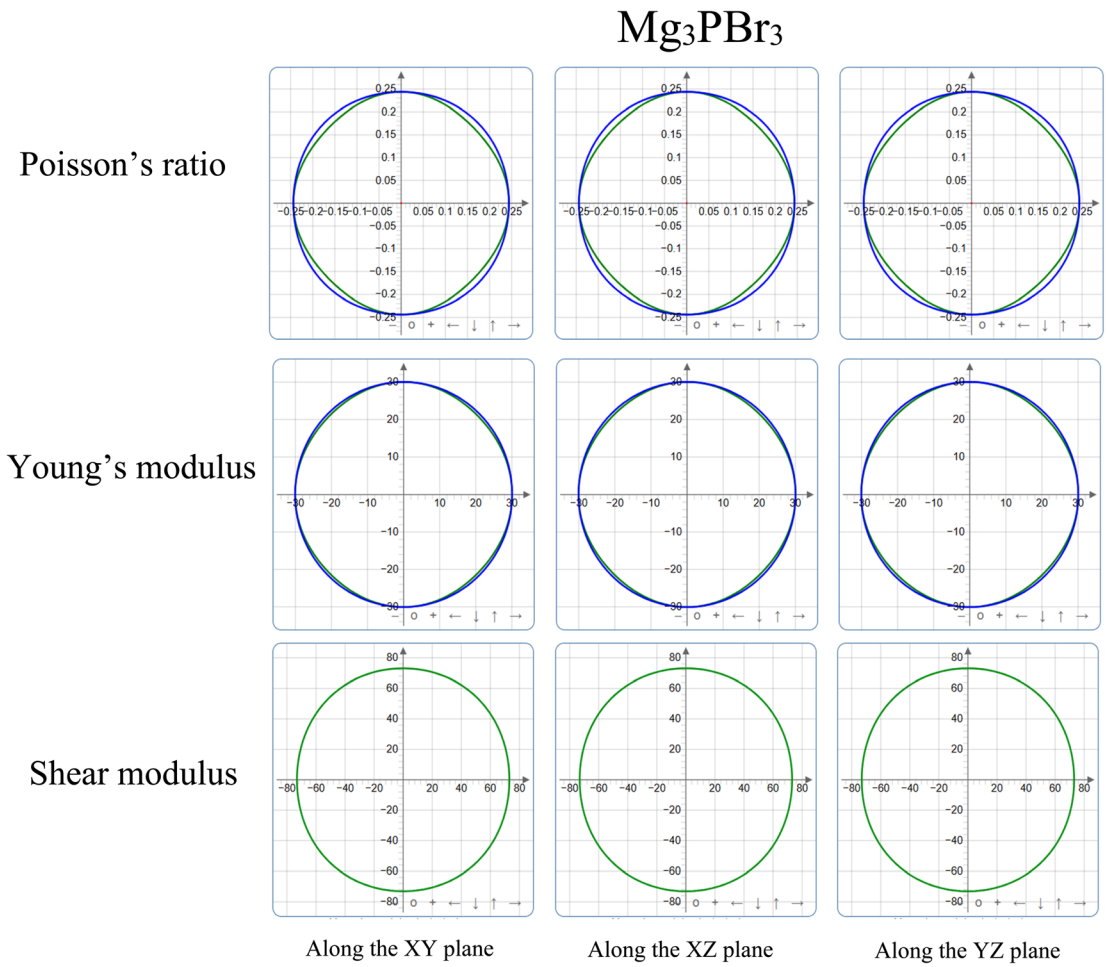

Fig. 16 The 2D illustration of Poisson ratio, Young modulus, and shear modulus of Mg_3PBr_3.

Table 6 Calculated thermal properties of the compound Mg_3PX_3 (X = Cl and Br)

Compound	V_t (m s^{-1})	V_l (m s^{-1})	V_m (m s^{-1})	K_{min} (W m^{-1} K^{-1})	K_{ph} (W m^{-1} K^{-1})	θ_D (K)	T_m (K)
Mg_3PCl_3	119 106.9	458 543	31 420.22	0.0459	50.98	304.44	1066.59
Mg_3PBr_3	92 654.17	550 426.2	24 493.77	0.0501	20.95	280.83	1065.67

K_{min} and show contribution from phonon transport to thermal conductivity. In comparison with Mg_3PBr_3, the value of K_{ph} is much higher, which points to a greater potential of Mg_3PCl_3 for heat transfer to the crystal lattice. This is consistent with its higher V_m suggesting better phonon transport behavior in the material. Notably, the values of the K_{min} are closer for both compounds, indicating the possibility of an atomic-scale restriction for thermal transport in both materials. As a result, Mg_3PCl_3 is more suitable for utilization in applications where it would act as a superior heatsink, in the form of thermal paste or electronic parts for example. Mg_3PBr_3 with lower K_{ph} values applicable for insulation. Also, low values of K_{ph} indicate that each material has a fundamental limitation regarding its ability to transfer heat per unit area, the limitation being firmly anchored in the atomic structure of a given material.

Debye temperature characterizes the upper limit of vibrational densities in a material and depends on its stiffness and lattice bonding strength.[82] Melting temperature (T_m) is the temperature at which the material changes from a solid to a liquid state and therefore its suitability for use under high temperatures.[83,84] The θ_D of Mg_3PCl_3 is 304.44 K, and the melting T_m is 1066.59 K, while for Mg_3PBr_3, the value of θ_D is 280.83 K and T_m is 1065.67 K. Due to the higher θ_D value for Mg_3PCl_3, which has a more rigid atomic bonding structure and stiffer lattice than the Mg_3PBr_3. Both materials have low melting points, around 1065 K, indicated to have comparably high-temperature stability. The graphical representation of the Debye temperature is shown Fig. 14. The slightly higher θ_D of Mg_3PCl_3 suggests efficient high heat resistance. The Debye temperature is essential in determining the lower temperature

heat capacity of a material and its expansion coefficient. The observed higher θ_D of Mg_3PCl_3 as compared to Mg_3PBr_3 indicates that it may have better thermal resistance and a lower coefficient of thermal expansion. This means that the two materials can be substituted for each other for use in high-temperature applications so long as other characteristics are desirable.

Mg_3PCl_3 shows superior results compared to Mg_3PBr_3 for sound velocity, lattice thermal conductivity, and Debye temperature properties and hence is considered to be more appropriate for high thermal conductivity and structural applications. The compound Mg_3PBr_3, although showing somewhat lower thermal stability, is also preferable in applications where the material with lower thermal conductivity is preferable. It was also noted that these two materials have similar melting features, which indicates that they have comparable properties under severe thermal conditions.

4. Conclusion

The study of photovoltaics focused on determining the physical properties and their suitable applications in various fields. This computation mainly focused on physical, structural, mechanical, optical, magnetic, thermal, and dynamic outcomes of the novel inorganic non-toxic Mg_3PX_3 photovoltaic compound. The whole computation was carried out with CASTEP code within the GGA-PBE functional. Other Hybrid functional like HSE06 are used to determine the bandgap of the photovoltaic compound. The structural stability cross checked by the negative formation enthalpy, tolerate tolerance factor, *etc.* The calculated direct band gap was 2.297 eV (GGA-PBE) and 3.093 eV (HSE06) 1.506 eV (GGA-PBE) and 2.187 eV (HSE06) for Mg_3PCl_3 and Mg_3PBr_3 respectively. The bandgap range suggests the semiconductor range and the photovoltaic compound are very suitable for the semiconductor sectors and optoelectronics sectors. The structural stability is validated by the mechanical calculations and the C_{44} elastic constant was found positive. Along with negative Cauchy pressure, Poisson's, and Paugh ratio the brittleness of the compound is observed which makes it applicable in the inner section of pressure vessel type application. This diamagnetic photovoltaic compound is suitable for magnetic field research and quantum mechanical sectors. The direction-dependent property is anisotropic for this compound from the output of the ELATE tool. This compound can be synthesized experimentally to show positive phonon spectra in the calculation. The Debye temperature is moderate for both of them and the low melting point and comparable high-temperature stability make this compound applicable in high-temperature applications. This whole study denotes that Mg_3PX_3 compounds offer exceptional physical features which makes them suitable applicants for photovoltaic optoelectronic and quantum mechanical use. Excellent optical phenomena like absorption and conductivity ensure their potential uses in photovoltaics and optical applications. The study of novel photovoltaic Mg_3PX_3 broadens the sector of research of photovoltaics and the potential found in this study is remarkable.

Data availability

Data will be available upon request.

Author contributions

Md. Bayjid Hossain Parosh: investigation, methodology, validation, data curation, formal analysis, writing – original draft. Md. Saiduzzaman: formal analysis, conceptualization, supervision, writing – original draft, reviewing and editing. Jahirul Islam: data curation, formal analysis, writing – review & editing. Nusrat Jahan Nisha & Istiak Ahmed Ovi: investigation, visualization, writing – original draft, data curation, reviewing and editing.

Conflicts of interest

The authors declare that they have no known competing financial interests or personal relationships that could have appeared to influence the work reported in this paper.

Acknowledgements

This work was performed at the Computational Materials Science Laboratory, Department of Materials Science and Engineering, Khulna University of Engineering & Technology (KUET), Bangladesh.

References

1 N. A. Noor, *et al.*, Shift of indirect to direct bandgap and thermoelectric response of the cubic BiScO3 via DFT-mBJ studies, *Mater. Sci. Semicond. Process.*, 2016, **49**, 40–47, DOI: 10.1016/j.mssp.2016.03.014.

2 A. A. Mubarak and A. A. Mousa, The electronic and optical properties of the fluoroperovskite BaXF3 (X= Li, Na, K, and Rb) compounds, *Comput. Mater. Sci.*, 2012, **59**, 6–13.

3 T. W. Kelley, *et al.*, Recent Progress in Organic Electronics: Materials, Devices, and Processes, *Chem. Mater.*, 2004, **16**(23), 4413–4422, DOI: 10.1021/cm049614j.

4 Scopus preview - Scopus - Document details - Insight into the physical properties of the inter-metallic titanium-based binary compounds, Accessed: Dec. 13, 2024. [Online]. Available: https://www.scopus.com/record/display.uri?eid=2-s2.0-85107208268&origin=inward.

5 A. Polman, M. Knight, E. C. Garnett, B. Ehrler and W. C. Sinke, Photovoltaic materials: Present efficiencies and future challenges, *Science*, 2016, **352**(6283), aad4424.

6 S. D. Stranks, *et al.*, Electron-Hole Diffusion Lengths Exceeding 1 Micrometer in an Organometal Trihalide Perovskite Absorber, *Science*, 2013, **342**(6156), 341–344, DOI: 10.1126/science.1243982.

7 J.-C. Zheng, C. H. A. Huan, A. T. S. Wee and M. H. Kuok, Electronic properties of CsSnBr3: studies by experiment and theory, *Surf. Interface Anal.*, 1999, **28**(1), 81–83, DOI: 10.1002/(SICI)1096-9918(199908)28:1<81::AID-SIA623>3.0.CO;2-D.

8 M. Green, E. Dunlop, J. Hohl-Ebinger, M. Yoshita, N. Kopidakis and X. Hao, Solar cell efficiency tables (version 57), *Prog. Photovolt.: Res. Appl.*, 2021, **29**(1), 3–15.
9 D. S. Ginley and D. Cahen, *Fundamentals of Materials for Energy and Environmental Sustainability*, Cambridge University Press, 2011.
10 H. J. Snaith, Perovskites: The Emergence of a New Era for Low-Cost, High-Efficiency Solar Cells, *J. Phys. Chem. Lett.*, 2013, **4**(21), 3623–3630, DOI: **10.1021/jz4020162**.
11 S. D. Stranks and H. J. Snaith, Metal-halide perovskites for photovoltaic and light-emitting devices, *Nat. Nanotechnol.*, 2015, **10**(5), 391–402, DOI: **10.1038/nnano.2015.90**.
12 F. Zhang, *et al.*, Brightly Luminescent and Color-Tunable Colloidal CH3NH3PbX3 (X = Br, I, Cl) Quantum Dots: Potential Alternatives for Display Technology, *ACS Nano*, 2015, **9**(4), 4533–4542, DOI: **10.1021/acsnano.5b01154**.
13 N.-G. Park, Perovskite solar cells: an emerging photovoltaic technology, *Mater. Today*, 2015, **18**(2), 65–72, DOI: **10.1016/j.mattod.2014.07.007**.
14 H.-J. Feng and Q. Zhang, Predicting efficiencies >25% A3MX3 photovoltaic materials and Cu ion implantation modification, *Appl. Phys. Lett.*, 2021, **118**(11), 111902, DOI: **10.1063/5.0039936**.
15 A. Ghosh, *et al.*, Investigating of novel inorganic cubic perovskites of A3BX3 (A=Ca, Sr, BP, As, X=I, Br) and their photovoltaic performance with efficiency over 28%, *J. Alloys Compd.*, 2024, **986**, 174097, DOI: **10.1016/j.jallcom.2024.174097**.
16 Md. A. Hossain, *et al.*, Investigation of the physical properties and pressure-induced band gap tuning of Sr3ZBr3 (Z = As, Sb) for optoelectronic and thermoelectric applications: A DFT - GGA and mBJ studies, *Results Eng.*, 2024, 103340, DOI: **10.1016/j.rineng.2024.103340**.
17 H. A. Abdulhussein, *et al.*, A comprehensive analysis of the structural, phonon, electronic, mechanical, optical, and thermophysical properties of cubic Ca3SbX3 (X = Cl, Br): DFT - GGA and mBJ studies, *Mater. Sci. Semicond. Process.*, 2025, **187**, 109133, DOI: **10.1016/j.mssp.2024.109133**.
18 S. Chahar, K. K. Mishra and R. Sharma, Investigation of Structural, Electronic, and Optical Characteristics of a Novel Perovskite Halide, Mg3AsCl3, for Electronic Applications, *Phys. Status Solidi B*, 2024, **261**(10), 2400171, DOI: **10.1002/pssb.202400171**.
19 I. K. G. G. Apurba, Md. R. Islam, Md. S. Rahman, Md. F. Rahman and J. Park, Tuning the physical properties of inorganic novel perovskite materials Ca3PX3 (X=I, Br and Cl): Density function theory, *Heliyon*, 2024, **10**(7), e29144, DOI: **10.1016/j.heliyon.2024.e29144**.
20 Md. F. Rahman, Md. H. Rahman, T. A. Galib, A. Habib and A. Irfan, A DFT-based computational study on a highly and lead-free inorganic new fluoroperovskite of Mg3PF3, *Phys. Lett. A*, 2024, **528**, 130027, DOI: **10.1016/j.physleta.2024.130027**.
21 R. Zhao, *et al.*, Microstructure and Mechanical Properties of TixNbMoTaW Refractory High-Entropy Alloy for Bolt Coating Applications, *Coatings*, 2025, **15**, 120, DOI: **10.3390/coatings15020120**.
22 J. P. Perdew, K. Burke and M. Ernzerhof, Generalized gradient approximation made simple, *Phys. Rev. Lett.*, 1996, **77**(18), 3865.
23 W.-J. Yin, T. Shi and Y. Yan, Unique Properties of Halide Perovskites as Possible Origins of the Superior Solar Cell Performance, *Adv. Mater.*, 2014, **26**(27), 4653–4658, DOI: **10.1002/adma.201306281**.
24 A. Babayigit, *et al.*, Assessing the toxicity of Pb- and Sn-based perovskite solar cells in model organism Danio rerio, *Sci. Rep.*, 2016, **6**, 18721, DOI: **10.1038/srep18721**.
25 M. Saiduzzaman, *et al.*, Band gap tuning of non-toxic Sr-based perovskites CsSrX3 (X = Cl, Br) under pressure for improved optoelectronic applications, *Mater. Today Commun.*, 2022, **34**, 105188, DOI: **10.1016/j.mtcomm.2022.105188**.
26 B.-H. Huang, Y.-F. Lai and Y.-H. Tang, Validity of DFT-based spin-orbit torque calculation for perpendicular magnetic anisotropy in iron thin films, *AIP Adv.*, 2023, **13**, 015034, DOI: **10.1063/9.0000481**.
27 N. J. Nisha, Md. B. Hossain Parosh, I. A. Ovi and Md. J. Islam, Investigation of electronic, optoelectronic, and mechanical properties of lead-free cubic perovskite compound using density functional theory, *AIP Adv.*, 2024, **14**(11), 115226, DOI: **10.1063/5.0232366**.
28 M. R. Hasan, I. Apon, I. Ovi and F. Zahra, Impact of Applied Pressure on Tin-Based Cubic Halide Perovskite ASnX3 (A = Li, Na and X = Cl, Br, and I) in Reference to Their Optoelectronic Applications, *Int. J. Energy Res.*, 2024, **2024**, 34, DOI: **10.1155/2024/8213804**.
29 H.-J. Feng and Q. Zhang, Predicting efficiencies >25% A 3 MX 3 photovoltaic materials and Cu ion implantation modification, *Appl. Phys. Lett.*, 2021, **118**, 111902, DOI: **10.1063/5.0039936**.
30 M. D. Hasan, I. A. Apon, I. A. Ovi and M. S. Haque, Calculations of the mechanical, optoelectronic, and magnetic properties of FrGeX3 (X = Cl, Br, I) under hydrostatic pressures based on first-principles theories, *AIP Adv.*, 2024, **14**(3), DOI: **10.1063/5.0201448**.
31 J. K. Rony, *et al.*, TlBX3 (B = Ge, Sn; X = Cl, Br, I): Promising non-toxic metal halide perovskites for scalable and affordable optoelectronics, *J. Mater. Res. Technol.*, 2024, **29**, 897–909, DOI: **10.1016/j.jmrt.2024.01.093**.
32 Phonon calculations—ASE documentation, Accessed: Jan. 11, 2025. [Online]. Available: **https://wiki.fysik.dtu.dk/ase/ase/phonons.html?form=MG0AV3**.
33 Formulations—Phonopy v.2.34.0, Accessed: Jan. 11, 2025. [Online]. Available: **https://phonopy.github.io/phonopy/formulation.html?form=MG0AV3**.
34 A. H. Harker, The physics of phonons: by Gyaneshwar P. Srivastava, Boca Raton, FL/Abingdon, UK, CRC Press, 2023, xxi+ 434 pp.,£ 180 (hardback), ISBN 978-0-367-68526-3. Scope: monograph. Level: advanced undergraduate, graduate, early stage researcher, *Contemp. Phys.*, 2022, **63**(4), 337.
35 P. Ding, Y. Zhu, Z. Han, L. Li, L. Zhang, Y. Cai, D. J. Singh, L. Zhang, W. Zhang, S. Shin and J. Yang, Coherent acoustic phonon dynamics facilitating acoustic

deformation potential characterization of Mg3Sb2, *Phys. Rev. B*, 2023, **108**(6), 064310.

36 R. S. Brokaw, Alignment Charts for Transport Properties, Viscosity, *Thermal Conductivity, and Diffusion Coefficients for Nonpolar Gases and Gas Mixtures at Low Density*, U.S. Government Printing Office, 1961.

37 M. Xing, B. Li, Z. Yu and Q. Chen, Elastic Anisotropic and Thermodynamic Properties of I-4m2-BCN, *Acta Phys. Pol. A*, 2016, **129**(6), 1124–1130, DOI: 10.12693/APhysPolA.129.1124.

38 A. E. Dixon, 23 - Review Of Solid State Physics, in *Solar Energy Conversion*, ed. A. E. Dixon and J. D. Leslie, Pergamon, 1979, pp. 773–784, DOI: 10.1016/B978-0-08-024744-1.50028-0.

39 C. Kittel and P. McEuen, *Introduction to Solid State Physics*. John Wiley & Sons, 2018.

40 P. YU and M. Cardona, *Fundamentals of Semiconductors: Physics and Materials Properties*. Springer Science & Business Media, 2010.

41 F. Brivio, A. B. Walker and A. Walsh, Structural and electronic properties of hybrid perovskites for high-efficiency thin-film photovoltaics from first-principles, *APL Mater.*, 2013, **1**(4), 042111, DOI: 10.1063/1.4824147.

42 J. Even, L. Pedesseau and C. Katan, Understanding quantum confinement of charge carriers in layered 2D hybrid perovskites, *ChemPhysChem*, 2014, **15**(17), 3733–3741.

43 W. Kohn and L. J. Sham, Self-consistent equations including exchange and correlation effects, *Phys. Rev.*, 1965, **140**(4A), A1133.

44 J. Heyd, G. E. Scuseria and M. Ernzerhof, Hybrid functionals based on a screened Coulomb potential, *J. Chem. Phys.*, 2003, **118**(18), 8207–8215.

45 A. V. Krukau, O. A. Vydrov, A. F. Izmaylov and G. E. Scuseria, Influence of the exchange screening parameter on the performance of screened hybrid functionals, *J. Chem. Phys.*, 2006, **125**(22), 224106.

46 A. Rezende, *et al.*, DFT Calculations for Structural, Electronic, and Magnetic Properties of ZnFe2O4 Spinel Oxide: The Role of Exchange-Correlation Functional, *Mater. Res.*, 2022, **25**, e20220219, DOI: 10.1590/1980-5373-mr-2022-0219.

47 A. Kuzubov, *et al.*, DFT investigation of electronic structures and magnetic properties of halides family MeHal3 (Me=Ti, Mo,Zr,Nb, Ru, Hal=Cl,Br,I) one dimensional structures, *J. Magn. Magn. Mater.*, 2016, **440**, 93–96, DOI: 10.1016/j.jmmm.2016.12.054.

48 R. M. Kusters, J. Singleton, D. A. Keen, R. McGreevy and W. Hayes, Magnetoresistance measurements on the magnetic semiconductor Nd0.5Pb0.5MnO3, *Phys. B*, 1989, **155**(1), 362–365, DOI: 10.1016/0921-4526(89)90530-9.

49 A. Oleaga, A. Salazar and D. Skrzypek, Critical behaviour of magnetic transitions in KCoF3 and KNiF3 perovskites, *J. Alloys Compd.*, 2015, **629**, 178–183, DOI: 10.1016/j.jallcom.2014.12.237.

50 S. H. Mikkelsen, B. Wied, V. Dashkovskyi, T. B. Lindhardt, L. Hirschler, J. M. Warnking, E. L. Barbier, D. Postnov, B. Hansen and E. Gutiérrez-Jiménez, Head holder and cranial window design for sequential magnetic resonance imaging and optical imaging in awake mice, *Front. Neurosci.*, 2022, **16**, 926828.

51 Md. S. Islam, *et al.*, An in-depth analysis of how strain impacts the electronic, optical, and output performance of the Ca3NI3 novel inorganic halide perovskite, *J. Phys. Chem. Solids*, 2024, **185**, 111791, DOI: 10.1016/j.jpcs.2023.111791.

52 H. J. Snaith, Perovskites: The Emergence of a New Era for Low-Cost, High-Efficiency Solar Cells, *J. Phys. Chem. Lett.*, 2013, **4**(21), 3623–3630, DOI: 10.1021/jz4020162.

53 J. Rony, M. Hasan, M. Rifat, M. Saiduzzaman and M. Islam, Pressure-induced DFT evaluation of MSnI3 (M = K, Rb) perovskites for electronic phase transition and enhanced optoelectronic utilization, *Comput. Theor. Chem.*, 2024, **1233**, 114512, DOI: 10.1016/j.comptc.2024.114512.

54 M. Roknuzzaman, K. (Ken) Ostrikov, H. Wang, A. Du and T. Tesfamichael, Towards lead-free perovskite photovoltaics and optoelectronics by ab-initio simulations, *Sci. Rep.*, 2017, **7**(1), 14025, DOI: 10.1038/s41598-017-13172-y.

55 S. Boucetta, Theoretical study of elastic, mechanical and thermodynamic properties of MgRh intermetallic compound, *J. Magnesium Alloys*, 2014, **2**(1), 59–63, DOI: 10.1016/j.jma.2014.04.001.

56 S. Saha, T. P. Sinha and A. Mookerjee, Structure, structural phase transitions, mechanical properties, defects, etc.-Electronic structure, chemical bonding, and optical properties of paraelectric BaTiO3, *Phys. Rev. B: Condens. Matter Mater. Phys.*, 2000, **62**(13), 8828–8834.

57 A. Ghosh, M. F. Rahman, M. R. Islam, M. S. Islam, M. Amami, M. K. Hossain and A. B. M. Ismail, Inorganic novel cubic halide perovskite Sr3AsI3: strain-activated electronic and optical properties, *Heliyon*, 2023, **9**(8), e19271.

58 M. A. Ali, R. Ullah, S. A. Dar, G. Murtaza, A. Khan and A. Mahmood, Modeling of structural, elastic, mechanical, acoustical, electronic and thermodynamic properties of XPdF3 (X = Rb, Tl) perovskites through density functional theory, *Phys. Scr.*, 2020, **95**(7), 075705, DOI: 10.1088/1402-4896/ab8eee.

59 Md. M. Rahaman, *et al.*, Mechanical, electronic, optical, and thermodynamic properties of orthorhonmbic LiCuBiO4 crystal: a first–priciples study, *J. Mater. Res. Technol.*, 2019, **8**(5), 3783–3794, DOI: 10.1016/j.jmrt.2019.06.039.

60 F. Zareef, M. Rashid, A. A. H. Ahmadini, T. Alshahrani, N. A. Kattan and A. Laref, Optoelectronic and thermoelectrical and mechanical properties of CdLu2X4 (X = S, Se) using first-principles calculations for energy harvesting applications, *Mater. Sci. Semicond. Process.*, 2021, **127**, 105695, DOI: 10.1016/j.mssp.2021.105695.

61 S. Kamran, K. Chen and L. Chen, Ab initio examination of ductility features of fcc metals, *Phys. Rev. B*, 2009, **79**(2), 024106, DOI: 10.1103/PhysRevB.79.024106.

62 Md. R. Talukder, S. Alam, M. Hasan, M. Sarker, Md. R. Islam and S. Ahmad, Indirect to Direct Band Gap Transition of ABI3 (A = Rb, Cs; B = Ca, Sr) Perovskites under Hydrostatic Pressure for Photovoltaic and Optoelectronic

Applications: A DFT Study, *Phys. B*, 2024, 416538, DOI: 10.1016/j.physb.2024.416538.

63 M. Born, On the stability of crystal lattices. I, *Math. Proc. Cambridge Philos. Soc.*, 1940, **36**(2), 160–172, DOI: 10.1017/S0305004100017138.

64 M. I. Ahmed, A. Biswas, T. I. Asif, M. Saiduzzaman and M. Islam, Hydrostatic pressure-induced transformations and multifunctional properties of Francium-based halide perovskite FrCaCl3: Insights from first-principles calculations, *Heliyon*, 2024, **10**, e34059, DOI: 10.1016/j.heliyon.2024.e34059.

65 Physical properties of CsSnM3 (M = Cl, Br, I): A first principle study, Request PDF. Accessed: Feb. 08, 2025. [Online]. Available: https://www.researchgate.net/publication/285993699_Physical_properties_of_CsSnM3_M_Cl_Br_I_A_first_principle_study.

66 M. Rahman, M. Rahman, T. A. Galib, Md. A. Habib and A. Irfan, A DFT-based computational study on a highly and lead-free inorganic new fluoroperovskite of Mg3PF3, *Phys. Lett. A*, 2024, 130027, DOI: 10.1016/j.physleta.2024.130027.

67 Md. T. Hossain, *et al.*, A Comprehensive DFT Investigation of Inorganic Halide Perovskites GaXCl3 (X = Ca, Sr, and Ba) for Optoelectronics Application, *Phys. B*, 2024, **690**, 416131, DOI: 10.1016/j.physb.2024.416131.

68 Md. R. Talukder, W. Sajal, S. Alam, F. Zahra and J. Islam, Tuning band gap and improving optoelectronic properties of lead-free halide perovskites FrMI3 (M= Ge, Sn) under hydrostatic pressure, *Solid State Commun.*, 2024, **396**, 115759, DOI: 10.1016/j.ssc.2024.115759.

69 M. Tariq, M. A. Ali, A. Laref and G. Murtaza, Anion replacement effect on the physical properties of metal halide double perovskites Cs2AgInX6 (X=F, Cl, Br, I), *Solid State Commun.*, 2020, **314–315**, 113929, DOI: 10.1016/j.ssc.2020.113929.

70 X. Liu and H. Fan, Electronic structure, elasticity, Debye temperature and anisotropy of cubic WO 3 from first-principles calculation, *R. Soc. Open Sci.*, 2018, **5**, 171921, DOI: 10.1098/rsos.171921.

71 Md. A. Islam, M. Rahaman and S. Sen, A comparative study of hydrostatic pressure treated environmentally friendly perovskites CsXBr3 (X = Ge/Sn) for optoelectronic applications, *AIP Adv.*, 2021, **11**, 75109, DOI: 10.1063/5.0057287.

72 G. Globočkilakić, S. Borojevic, D. Čiča and B. Sredanovic, Development of application for analysis of machinability index, *Tribol. Ind.*, 2009, **31**, 57–60.

73 M. R. Talukder, W. R. Sajal, M. S. Alam and J. Islam, Tuning band gap and improving optoelectronic properties of lead-free halide perovskites FrMI3 (M= Ge, Sn) under hydrostatic pressure, *Solid State Commun.*, 2025, **396**, 115759.

74 D. H. Chung and W. R. Buessem, The Elastic Anisotropy of Crystals, *J. Appl. Phys.*, 1967, **38**(5), 2010–2012.

75 M. Hasan, K. Hossain, S. Mitro, M. Rasheduzzaman, J. Modak and M. Rayhan, Structural, mechanical, electronic, and anisotropic properties of niobium-doped strontium ferrite: First-principle calculations, *Appl. Phys. A*, 2021, **127**, 1–9, DOI: 10.1007/s00339-020-04219-5.

76 Md. Rasheduzzaman, K. M. Hossain, S. K. Mitro, M. A. Hadi, J. K. Modak and Md. Z. Hasan, Structural, mechanical, thermal, and optical properties of inverse-Heusler alloys Cr2CoZ (Z = Al, In): A first-principles investigation, *Phys. Lett. A*, 2021, **385**, 126967, DOI: 10.1016/j.physleta.2020.126967.

77 M. E. Fine, L. D. Brown and H. L. Marcus, Elastic constants versus melting temperature in metals, *Scr. Metall.*, 1984, **18**(9), 951–956, DOI: 10.1016/0036-9748(84)90267-9.

78 R. Bortfeld, Approximations To The Reflection And Transmission Coefficients Of Plane Longitudinal And Transverse Waves, *Geophys. Prospect.*, 1961, **9**, 485–502, DOI: 10.1111/j.1365-2478.1961.tb01670.x.

79 S. J. Schön, Chapter 9 – Thermal Properties, in *Handbook of Petroleum Exploration and Production*, ed. J. H. Schön, Physical Properties of Rocks, Elsevier, 2011, vol. 8, pp. 337–372, DOI: 10.1016/S1567-8032(11)08009-8.

80 G. A. Slack, The Thermal Conductivity of Nonmetallic Crystals, in *Solid State Physics*, ed. H. Ehrenreich, F. Seitz, and D. Turnbull, Academic Press, 1979, vol. 34, pp. 1–71, DOI: 10.1016/S0081-1947(08)60359-8.

81 D. G. Cahill, S. K. Watson and R. O. Pohl, Lower limit to the thermal conductivity of disordered crystals, *Phys. Rev. B:Condens. Matter Mater. Phys.*, 1992, **46**(10), 6131.

82 R. K. Fitzgerel and F. H. Verhoek, The law of Dulong and Petit, 1960.

83 Q. J. Hong, Melting temperature prediction via first principles and deep learning, *Comput. Mater. Sci.*, 2022, **214**, 111684.

84 Md. B. H. Parosh, *et al.*, DFT Investigations of Non-Toxic Perovskites RbZnX (X = F, Cl, and Br): Analyzing the Structural, Electrical, Optical, Mechanical, and Thermodynamic Properties for Suitable Optoelectronic Applications, *Int. J. Quantum Chem.*, 2025, **125**(4), e70014, DOI: 10.1002/qua.70014.